



## Climate change has altered zooplankton-fuelled carbon export in the North Atlantic

**Brun, Philipp Georg; Stamieszkin, Karen ; Visser, Andre W.; Licandro, Priscilla; Payne, Mark; Kiørboe, Thomas**

*Published in:*  
Nature Ecology & Evolution

*Link to article, DOI:*  
[10.1038/s41559-018-0780-3](https://doi.org/10.1038/s41559-018-0780-3)

*Publication date:*  
2019

*Document Version*  
Peer reviewed version

[Link back to DTU Orbit](#)

*Citation (APA):*  
Brun, P. G., Stamieszkin, K., Visser, A. W., Licandro, P., Payne, M., & Kiørboe, T. (2019). Climate change has altered zooplankton-fuelled carbon export in the North Atlantic. *Nature Ecology & Evolution*, 3(3), 416-423. <https://doi.org/10.1038/s41559-018-0780-3>

---

### General rights

Copyright and moral rights for the publications made accessible in the public portal are retained by the authors and/or other copyright owners and it is a condition of accessing publications that users recognise and abide by the legal requirements associated with these rights.

- Users may download and print one copy of any publication from the public portal for the purpose of private study or research.
- You may not further distribute the material or use it for any profit-making activity or commercial gain
- You may freely distribute the URL identifying the publication in the public portal

If you believe that this document breaches copyright please contact us providing details, and we will remove access to the work immediately and investigate your claim.

1 **Climate change has altered zooplankton-fuelled carbon export in**  
2 **the North Atlantic**

3 Philipp Brun<sup>1,2,\*</sup>, Karen Stamieszkin<sup>3,4</sup>, Andre W. Visser<sup>1</sup>, Priscilla Licandro<sup>5,6,7</sup>, Mark R.  
4 Payne<sup>1</sup>, and Thomas Kiørboe<sup>1</sup>

5 <sup>1</sup>Centre for Ocean Life, National Institute of Aquatic Resources, Technical University of  
6 Denmark, Kgs. Lyngby, Denmark

7 <sup>2</sup>Dynamic Macroecology Group, WSL, Zuercherstrasse 111, CH-8903, Birmensdorf,  
8 Switzerland

9 <sup>3</sup>School of Marine Sciences, 360 Aubert Hall, University of Maine, Orono, Maine 04469-  
10 5706, USA

11 <sup>4</sup>Bigelow Laboratory for Ocean Sciences, 60 Bigelow Drive, East Boothbay, Maine USA

12 <sup>5</sup>Sir Alister Hardy Foundation for Ocean Science, The Laboratory, Citadel Hill, Plymouth  
13 PL1 2PB, United Kingdom

14 <sup>6</sup>Plymouth Marine Laboratory, Prospect Place, The Hoe, Plymouth, PL1 3DH, United  
15 Kingdom

16 <sup>7</sup>Stazione Zoologica Anton Dohrn, Villa Comunale, 80121 Napoli, Italy

17

18 \*Correspondence to: Philipp Brun (philipp.brun@wsl.ch)

19

20           **Introductory paragraph**

21           Marine plankton have been conspicuously affected by recent climate change,  
22 responding with profound spatial relocations, and shifts in the timing of their seasonal  
23 occurrence. These changes directly impact the global carbon cycle by altering the transport of  
24 organic material from the surface ocean to depth, with consequences that remain poorly  
25 understood. We investigated how distributional and abundance changes of copepods, the  
26 dominant group of zooplankton, have affected biogenic carbon cycling. We used trait-based,  
27 mechanistic models to estimate the magnitude of carbon transported downward through  
28 sinking fecal pellets, daily vertical migration, and seasonal hibernation at depth. From such  
29 estimates for over 200,000 community observations in the northern North Atlantic we found  
30 carbon flux increases along the northwestern boundary of the study area and decreases in the  
31 open northern North Atlantic during the past 55 years. These changes in export were  
32 primarily associated with changes in copepod biomass, which were driven by shifting  
33 distributions of abundant, large-bodied species. Our findings highlight how recent climate  
34 change has fundamentally impacted downward carbon transport by altering copepod  
35 community structure, and demonstrate how carbon fluxes through plankton communities can  
36 be mechanistically implemented in next-generation biogeochemical models with size-  
37 structured representations of zooplankton communities.

38

39

## 40 **Main text**

### 41 **Introduction**

42 The various processes by which organic material is transported from the surface ocean  
43 to depth are collectively called the biological pump and remove roughly the same amount of  
44 carbon from the atmosphere as humanity has been emitting in recent years<sup>1,2</sup>. Surface-layer  
45 copepods contribute to the biological pump through the production of sinking fecal pellets,  
46 shed exoskeletons and carcasses, and by conducting vertical migrations<sup>3</sup>. Fecal pellets are  
47 compact aggregates of organic material with dimensions proportional to the size of the  
48 organism producing them<sup>4,5</sup>. Small fecal pellets produced by small copepods sink more  
49 slowly and are thus subject to a greater degree of remineralization, delivering proportionately  
50 less carbon to depth. Zooplankton fecal pellets can reach depths of 1000 meters or more, and  
51 are commonly found in sediment traps throughout the world's oceans, contributing to the  
52 passive organic particle flux in highly variable fractions (0-100%)<sup>5</sup>.

53 Copepods transport carbon actively by conducting daily vertical migrations (DVMs)  
54 and seasonal migrations. Zooplankton feeding in the surface layer at night, and seeking  
55 refuge at depth during the day leads to DVM<sup>6</sup> (Fig. 1a). Such migrations are widespread and  
56 most beneficial when food availability and predation pressure in surface waters are high,  
57 particularly for larger organisms that swim faster and more efficiently<sup>7</sup>. During daily vertical  
58 migrations, carbon consumed near the sea surface is respired and defecated at depth<sup>8,9</sup>. The  
59 magnitude of this form of carbon transport ranges up to 70% of passive organic particle  
60 fluxes<sup>7</sup> and reaches a few hundred meters of depth at maximum<sup>10</sup>.

61 Copepods conduct seasonal vertical migrations to hibernate at depth<sup>11</sup>, typically  
62 descending hundreds to thousands of meters. This strategy is found in polar and subpolar  
63 environments with severe winters. In the North Atlantic it is a conspicuous behavior in three  
64 *Calanus* species<sup>12</sup>. Carbon transport through seasonal migration results from respiration and  
65 mortality at depth (Fig. 1b). In regions where hibernating *Calanus* species are highly  
66 abundant, the magnitude of this process is comparable to passive organic particle flux<sup>13-15</sup>.

## 67 **Results and Discussion**

68 We used an optimal behavior model<sup>7</sup> to estimate the extent of DVM for copepods  
69 observed by the Continuous Plankton Recorder (CPR) program<sup>16,17</sup> during the period 1960-  
70 2014. Optimal behavior models assume that the behavior of naturally selected organisms is  
71 optimal with respect to evolutionary fitness, and thus predictable if the effects of  
72 environmental characteristics on fitness are known (see Methods). Observations were taken at  
73 approximately 7 m depth and include adults, near-adults, and early life stages when available,  
74 of the 45 taxa comprising >99% of the biomass sampled (Supplementary Table 1). DVM  
75 depth and duration were estimated for each taxon based on food availability, temperature,  
76 light intensity, and body size. On the community level, we forced DVM duration to match  
77 observed differences in day- and night-time biomass (Supplementary Figure 3). The resulting  
78 DVM depth estimates varied within a conservative but realistic<sup>10</sup> range (Supplementary  
79 Figure 4).

80 From these DVM estimates, we derived fecal pellet and DVM fluxes out of the upper  
81 mixed layer. We assumed that copepods produce fecal pellets in response to feeding in the  
82 surface layer, and that copepod body size determines pellet size, and thus sinking velocity  
83 and flux attenuation<sup>4</sup>. DVM flux was estimated as the sum of fecal pellets released during

84 migration<sup>7</sup> and respiration below the local mixed layer . Furthermore, we accounted for the  
85 effect of local temperature on feeding, respiration and remineralization rates (see Methods).

86         Spatiotemporal interpolations of fecal pellet and DVM fluxes at local mixed layer  
87 depth showed distinct spatial patterns and a strong seasonal signal (Fig. 2). High flux areas  
88 included the northwestern North Atlantic around the mouth of the Labrador Sea (Fig. 2a,b),  
89 where copepod biomass and average body size were high (Supplementary Figure 5). Fecal  
90 pellet fluxes were also high in the northern European and eastern North American shelf seas,  
91 despite considerably smaller average body size. In the North Sea, for example, the large  
92 population size of small copepods (Supplementary Figure 5) compensated for high  
93 remineralization loss caused by slow average fecal pellet sinking velocity<sup>18</sup>. Integrated over  
94 the entire area, carbon transport through sinking fecal pellets and DVM peaked in July, and  
95 had a second, smaller peak in September (Fig. 2c). Flux timing in the open ocean followed a  
96 south-north gradient, reaching 50% of total annual flux in May at 40°N, and about 2 months  
97 later at 60°N (Fig. 2d). In shallow, coastal areas with ample food and a high fraction of the  
98 copepod community hatching from resting eggs (Supplementary Figure 5), median annual  
99 flux was reached even later (July to August).

100         From 1960 to 2014 distinct changes in fecal pellet and DVM fluxes occurred across  
101 large parts of the study area. These fluxes have increased along the northern and northwestern  
102 boundary from Iceland to the Gulf of Maine, and have decreased across much of the open  
103 northern North Atlantic and the European Shelf Seas (Fig. 3a,b). During the past two  
104 decades, net primary production has also increased at high latitudes (Supplementary Figure  
105 10), due to warming and reduced sea ice coverage<sup>19,20</sup>. However, the spatial patterns of these  
106 changes were not strongly linked to changes in flux (see Supplementary Results). Trends in  
107 seven focal areas with high sampling effort highlight the spatial variability of change in

108 fluxes over the time series (Fig. 3c, d). We found distinct negative trends in the sum of the  
109 two fluxes in the areas “Iceland” and “Celtic S”, while in the area “North S” the trend was  
110 slightly positive (Fig. 3c, d). Interestingly, the trends were linked to changes in the timing of  
111 50% annual flux, with earlier timings being associated with decreasing annual fluxes.  
112 Overlaying the general trend, flux changes also showed considerable small-scale variation in  
113 magnitude and sometimes direction (Fig. 3a,b). Potentially, this variability resulted from the  
114 patchy distribution of copepod populations and it may have been amplified by the  
115 heterogeneous response of plankton species distributions to climate change<sup>19,21,22</sup> and  
116 consequent trophic mismatches<sup>23</sup>.

117 We estimated the duration of seasonal migrations and abundance of migrating  
118 populations for the hibernating species *Calanus finmarchicus*, *C. hyperboreus*, and *C.*  
119 *glacialis* from spatiotemporal interpolations of night-time observations, and used them to  
120 calculate hibernation fluxes (respiration and mortality during overwintering), which we  
121 assumed to be restricted to areas of at least 500 meters depth (see Methods). Significant  
122 hibernation fluxes were confined to the northwestern half of the investigated area, peaking  
123 around the mouth of the Labrador Sea (Fig. 4a). This pattern resembled the distribution of *C.*  
124 *finmarchicus*, the most abundant of the hibernating species. The changes in hibernation fluxes  
125 between 1960 and 2014 were similar to those of fecal pellet and DVM fluxes, showing an  
126 increase along the northwestern boundary of the investigated area and a decrease further  
127 southeast. However, the area of hibernation flux increase was somewhat larger, including the  
128 focal area “Iceland” (Fig. 4c). In contrast to the general trend, hibernation fluxes declined  
129 during the most recent period in the “Labrador” and “Irminger” regions. This may ultimately  
130 be linked to changes in the distribution of *C. finmarchicus* populations, which have been  
131 related to large scale hydroclimatic oscillations, such as the North Atlantic Oscillation

132 (NAO), that control ocean currents and in turn the advection of the species<sup>24</sup>. Indeed the  
133 NAO Index was particularly low during the period 2004-2014, a condition that has been  
134 related to enhanced intrusion of subarctic water into the Scotian Shelf/Gulf of Maine region  
135 and associated declines in local *C. finmarchicus* populations<sup>24</sup>.

136         Based on the flux estimates presented here, fecal pellet production represents the most  
137 important form of carbon transport by surface-layer copepods (Supplementary Figure 6). At  
138 mixed layer depth, fecal pellet flux was on average about ten times higher than DVM flux  
139 with highest relative differences in the shelf seas, where the fraction of migrating biomass  
140 was low, and in the southern part of the investigated area, where organisms were smaller and  
141 tended to remain at shallower depths (Supplementary Figures 4, 5). At 500 meters depth, the  
142 magnitudes of mean fecal pellet flux (including the contribution of abundant juvenile taxa)  
143 and mean hibernation flux (ignoring the contribution of juveniles) were similar. Hibernation  
144 flux transported more carbon to depth along the northwestern boundary of the study area,  
145 while fecal pellet flux dominated in the other parts.

146         We performed a sensitivity analysis to assess which of the temporally-resolved model  
147 inputs (i.e., copepod biomass, total abundance and abundance of key species, body size and  
148 temperature) most influenced the observed changes in carbon fluxes. Overall, changes in  
149 biomass correlated most strongly with changes in the fluxes modeled, with abundant, large-  
150 bodied species playing a key role (Fig. 5). A strong link between copepod biomass and  
151 carbon transport likely also exists for the poorly understood but potentially significant  
152 contributions from sinking carcasses and shed exoskeletons<sup>3</sup>. In contrast to the high  
153 spatiotemporal variations of biomass, mean copepod body size showed modest variability  
154 (Supplementary Figures 5, 7), and overall its temporal changes correlated less with changes  
155 in modeled carbon fluxes (Fig. 5). However, the relative importance of changes in body size



156 increased for fecal pellet fluxes estimated at greater depths. The distributions of *C.*  
157 *finmarchicus* and *C. hyperboreus* are known to have shifted in response to climate change<sup>25</sup>.  
158 The significant positive correlations between their relocations and shifts in the modeled  
159 carbon fluxes (Fig. 5) highlight how strongly relocations of dominant species can affect the  
160 climate system.

161         The correlations between changes in copepod biomass and changes in flux  
162 magnitudes were consistently positive across all focal areas at the  $p \leq 0.01$  level (Fig. 5),  
163 while the relationships of changes in sea surface temperature and body size with flux changes  
164 were more variable in space. Links between flux changes and changes in sea surface  
165 temperature were positive overall, as expected from our temperature-dependent formulation  
166 of feeding and metabolic rates, but in several focal areas, this relationship was not found.  
167 This result is not surprising as while increasing temperature has a direct, positive effect on  
168 copepod metabolism, it is often associated with stratification-driven nutrient limitation and  
169 smaller community body size<sup>3</sup> that have negative effects on community production and  
170 carbon export<sup>26</sup>. In the “Labrador” region, where changes in fluxes show a close positive link  
171 to changes in body size, decreasing community size structure during warm periods may have  
172 compensated for flux increases from enhanced metabolism, or, as in the case of mixed layer  
173 fecal pellet fluxes, even changed the sign to significant negative relationships between  
174 temperature changes and flux changes

175         While the spatial and temporal *patterns* identified here can be considered  
176 representative, our surface layer-based estimates of flux *magnitudes* are far smaller than those  
177 of depth-integrated assessments. Globally, zooplankton fecal pellets may constitute 40% of  
178 passive organic particle fluxes<sup>3</sup> and at high latitudes copepods may transport even more

179 carbon through seasonal migrations<sup>13–15</sup>. Our estimated total contribution of surface-layer  
180 copepods was  $0.2 \text{ gC m}^{-2} \text{ y}^{-1}$  at mixed layer depth which is much less than the estimated 29  
181  $\text{gC m}^{-2} \text{ y}^{-1}$  removed by the biological pump in the North Atlantic<sup>2</sup>. This is not surprising, as  
182 we only investigated the contribution of copepods in the top 14 meters, for which we  
183 considered our observational data to be representative. Consequently, for example our  
184 estimates of overwintering *C. finmarchicus* populations in the Labrador Sea were 53 times  
185 lower than hibernating populations counted at depth<sup>13</sup>. Nevertheless, the spatiotemporal  
186 patterns we identified in the surface waters are indicative for the layers below, as most taxa  
187 have connected populations spreading over wide depth ranges<sup>27</sup>. In the future, depth-  
188 integrated estimates of the zooplankton contribution to biogenic carbon flux may be enabled  
189 by increasingly available data from *in-situ* imaging surveys<sup>28</sup>.

190         The biological pump is the result of the complex interplay of biological, chemical, and  
191 physical processes and is currently not understood sufficiently well to derive clear  
192 expectations of its response to future climate change<sup>29,30</sup>. Even modeling the comparably  
193 well-understood contribution of surface-layer copepods required several limiting assumptions  
194 that we discuss in depth in the Supplementary Discussion. One key uncertainty, for instance,  
195 comes from copepod coprophagy – the feeding on fecal pellets with complex effects on their  
196 remineralization and sinking behavior<sup>5</sup>. While we implicitly included coprophagy through an  
197 observation-based formulation of fecal pellet remineralization rates, we could not account for  
198 its spatiotemporal variability. We therefore examined to what extent coprophageous taxa  
199 (*Oithona* and *Oncaea*)<sup>5</sup> may affect spatial patterns in surface-layer fecal pellet concentration  
200 and, hence, flux (see Supplementary Results). As the concentration of sinking fecal pellets  
201 was considerably lower than the concentration of phytoplankton, unselective feeding on  
202 pellets vs phytoplankton may have reduced fecal pellet concentration only little, with the

203 greatest impacts in shelf seas and in the southern oceanic part of the study area  
204 (Supplementary Figure 9). As expected, coprophagy had the least impact in areas with high  
205 fluxes and large mean community body size. Given current knowledge, it is not possible to  
206 estimate the contribution of integrated zooplankton coprophagy on fecal pellet fluxes.

207         In summary, we used a complex, mechanistic modeling framework combined with an  
208 unparalleled long-term dataset to study the key pathways by which surface-layer copepods  
209 transport carbon to depth, and found robust and significant north-westward shifts in North  
210 Atlantic carbon fluxes, driven by changes in biomass distributions and copepod community  
211 structure. While the northern North Atlantic has the highest data coverage, future research  
212 should also investigate other hotspots of zooplankton carbon export, such as the Nordic  
213 Seas<sup>13,14</sup> and the Southern Ocean<sup>15</sup>. Building on the trait-based approach and evolutionary  
214 rationale, our modeling framework has the generality to be readily applied in such systems.  
215 Moreover, it can be incorporated into next-generation biogeochemical models to formalize  
216 the fluxes through size-structured representations of zooplankton communities, ultimately  
217 reducing the uncertainty of climate prognoses.

218

## 219 **Methods**

### 220 **Overview**

221 The analyses consisted of three steps: first we estimated fecal pellet fluxes, DVM  
222 fluxes, and hibernation fluxes using mechanistic models and spatiotemporal interpolation  
223 techniques; second, we analyzed various spatial and temporal summary statistics from these  
224 estimates; finally, we investigated the role of potential drivers of the temporal flux changes  
225 observed.

226 We used the same framework to estimate fecal pellet and DVM fluxes, and estimated  
227 hibernation fluxes separately. Fecal pellet and DVM flux estimates were based on an optimal  
228 behavior model assessing the trade-off between feeding opportunity and predation risk for  
229 copepods in the surface layer. Copepods were assumed to have the choice between feeding in  
230 the surface layer and hiding in deeper, darker layers where predation risk gets increasingly  
231 lower. We assumed copepods to choose to migrate until the marginal energetic costs for  
232 swimming and lost feeding opportunity level off with the marginal gain from lower mortality  
233 - the behavior yielding highest expected fitness. The larger a copepod, the more efficiently it  
234 feeds<sup>31</sup> and swims<sup>7</sup> and thus the deeper and longer it can afford to migrate. From the optimal  
235 behavior estimates, fecal pellet and DVM fluxes were estimated individually for each taxon  
236 and observation, summed up, and interpolated in space and time.

237 *Calanus finmarchicus*, *C. hyperboreus* and *C. glacialis* are the main species  
238 conducting seasonal hibernation in the North Atlantic. To quantify the carbon fluxes  
239 originating from this behavior, we first produced monthly abundance climatologies for each  
240 combination of hibernating species and 11-year period investigated by interpolating

241 observations in space and time. Then, we used these climatologies to derive the abundance of  
242 migrating individuals as well as the duration of their diapause. Finally, we estimated  
243 hibernation fluxes as the sum of respiration and mortality at depth, integrated over the  
244 duration of the diapause. Respiration rates were assumed to depend on local temperature and  
245 on the body size of the organisms<sup>14</sup>.

246       Spatially resolved estimates for fecal pellet-, DVM-, and hibernation-fluxes – in the  
247 former two cases with additional seasonal resolution - were produced for five eleven-year  
248 periods. From these estimates we calculated annual means, total magnitude, phenology as  
249 well as decadal trends. Finally, we investigated how decadal trends in the flux estimates are  
250 linked to changes in temperature, copepod biomass, total copepod abundance and abundance  
251 of important taxa, and mean community body size. All analyses were conducted in the R  
252 environment<sup>32</sup>.

## 253       **Data**

### 254       ***Copepod community observations***

255       We used Continuous Plankton Recorder (CPR) observations from 1960 to 2014  
256 amounting to over 219,000 observations of 45 copepod taxa resolved in abundance classes<sup>17</sup>  
257 (Supplementary Table 1). Observed life stages comprised adults and copepodites V. For  
258 *Calanus*, *Metridia*, *Paracalanus* and *Pseudocalanus* species, younger copepodite stages were  
259 also included.

260       We analyzed temporal trends of carbon fluxes based on five periods by splitting the  
261 observational data into the subsets 1960-1970, 1971-1981, 1982-1992, 1993-2003, and 2004-  
262 2014. The spatial extent of the analyses was confined to the area of regular CPR sampling,

263 which we defined as pixels with a low standard deviation of spatiotemporal interpolations  
264 (see below). Furthermore, we defined seven focal areas with high sampling frequency for in-  
265 depth analyses (see Figs. 3, 4 and 5). These areas encompassed 8000 km<sup>2</sup> (except “Central A”  
266 covered 32,000 km<sup>2</sup>) and were of rectangular shape with an aspect ratio of 2:1 when mapped  
267 in geographic space. The areas “North S”, “Celtic S”, and “Newfoundl.” were shallower than  
268 500 meters and therefore not in the area of expected hibernation fluxes. The vertical extent of  
269 the study included the top 14 m of the water column, for which we assumed the CPR samples  
270 (taken at about 7 m depth) to be representative<sup>4</sup>.

## 271 ***Environment***

272 In order to estimate carbon fluxes, we needed information on temperature, food  
273 availability, water turbidity, and the depth of the mixed layer. For temperature ( $T$ ) we used  
274 data from both the World Ocean Atlas<sup>33</sup> and the Hadley Centre for Climate Prediction and  
275 Research<sup>34</sup>. Data from the World Ocean Atlas consist of six roughly decadal climatologies  
276 covering the periods 1955-1964, 1965-1974, 1975-1984, 1985-1994, 1995-2004, and 2005-  
277 2012, with 1°×1° horizontal resolution, and a vertical resolution of 5 and 25 m for 0-100 and  
278 100-500 m depth, respectively. Temperatures in the years 2013 and 2014 were approximated  
279 with the most recent climatology. We used local polynomial regression fitting to derive  
280 smooth local depth profiles for the optimal behavior models, and assumed the November-to-  
281 February averages of local temperature at 500 meters to represent the conditions experienced  
282 during hibernation at depth. In order to obtain accurate estimates of temperature changes  
283 throughout the study period, we also used the annually resolved sea surface temperature  
284 product HadISST1 from the Hadley Centre (1°×1° horizontal resolution).

285 Food availability was approximated based on phytoplankton biomass. We used size-  
286 resolved phytoplankton biomass estimates<sup>35</sup> to account for the fact that copepods cannot

287 directly feed on pico-phytoplankton. Phytoplankton biomass available to copepods was  
288 assumed to include microplankton and nanoplankton plus one tenth of the estimated  
289 picoplankton biomass. The latter term was included because 10% of the picoplankton  
290 biomass may be assimilated by heterotrophic flagellates, on which copepods can feed. We  
291 used an average monthly climatology of available phytoplankton biomass that was based on  
292 the years 1997 to 2010 and aggregated to  $0.5^\circ \times 0.5^\circ$  horizontal resolution. Water turbidity was  
293 represented by the diffuse attenuation coefficient of the downwelling irradiance at 490 nm  
294 (KD490) as available on the GlobColour website (<http://www.globcolour.info/>). We  
295 aggregated the monthly estimates from 1998 to 2014 to produce a climatology with  
296  $0.25^\circ \times 0.25^\circ$  horizontal resolution. For mixed layer depth (*MLD*) we used one monthly  
297  $0.5^\circ \times 0.5^\circ$  climatology to cover all observations<sup>36</sup>. Elevation data, used to constrain areas  
298 suitable for seasonal dormancy and to illustrate topography in the maps, was derived from the  
299 ETOPO1 Global Relief Model<sup>37</sup>.

### 300 ***Copepod dimensions***

301 To estimate migration behavior and carbon fluxes, we needed information on copepod  
302 body size. We compiled data on prosome length (*PL*), prosome width, and aspect ratio ( $\eta$ )  
303 from various sources (Supplementary Table 1), and computed copepod volume (*V*) as<sup>38</sup>

$$304 \quad V = \frac{4}{3} \pi \left(\frac{PL}{2}\right)^3 \eta^2 \quad (1)$$

305 and carbon mass ( $m_c$ ) from the empirical relationship<sup>31</sup>

$$306 \quad \log(m_c) = -0.93 + 0.95 \times \log(m_w) \quad (2)$$

307 where  $m_w$  is wet mass which we estimated assuming a copepod density of  $1 \text{ g cm}^{-3}$ . For a few  
308 species, information on aspect ratio was not available and estimated based on information  
309 from other taxa considered (see Supplementary Table 1 for details).

## 310           **Statistics**

311           We used statistics to constrain our mechanistic carbon flux models with data, to  
312 interpolate variables in space and time, to investigate temporal trends, and to investigate links  
313 between decadal changes in fluxes and potential drivers. To this end we employed  
314 spatiotemporal models, linear regression, quantile regression, and hypothesis testing.

### 315           ***Spatiotemporal interpolations***

316           We made spatiotemporal interpolations using the Integrated Nested Laplace  
317 Approximation (INLA) approach to model the distribution of average DVM duration, carbon  
318 fluxes, biomass, abundance, and equivalent spherical radius. The INLA approach is a  
319 computationally-efficient, Bayesian statistical tool that is particularly powerful in handling  
320 spatial and spatiotemporal correlation structures<sup>39,40</sup>. We assumed the modeled distributions  
321 to be isotropic, stationary Gaussian Fields and used the Stochastic Partial Differential  
322 Equation approach on discrete mesh points covering the investigated area (Supplementary  
323 Figure 1) for the interpolations. Furthermore, we exploited the seasonal autocorrelation in the  
324 data to produce well-informed climatologies. To this end, we assumed an autoregressive  
325 relation with the closest neighbors between the monthly time steps (AR1 process). A detailed  
326 description of the set-up of the spatiotemporal models is provided in the Supplementary  
327 Methods.

### 328           ***Regressions for temporal trends***

329           We used linear regressions to estimate temporal trends in carbon fluxes over the  
330 periods investigated. Quantile regression was used to identify trend lines in for parameters  
331 that were resampled from a posterior distribution; otherwise simple linear regression was  
332 employed.



333 ***Hypothesis testing***

334 *Hibernating population and diapause duration*

335 In order to estimate hibernation fluxes, we needed spatially-resolved information on  
336 the abundance of the hibernating individuals, as well as on the duration of their diapause. We  
337 obtained this information from the spatiotemporal interpolations of the abundance of the  
338 hibernating species. In order to estimate the duration of the diapause, a pixel-wise hypothesis-  
339 testing approach was employed.

340 The hibernating *Calanus* species are known to have diapause durations that vary in  
341 space. *C. finmarchicus* has been observed to be hibernating between four and seven months<sup>13</sup>,  
342 while the maximum hibernation duration for *C. hyperboreus* ranges up to eight months<sup>14</sup>.  
343 From this information we assumed *C. finmarchicus* and, due to its similar size, *C. glacialis* to  
344 be hibernating between four and seven months, and *C. hyperboreus* between five and eight  
345 months. Furthermore, we assumed that diapause always included the months December and  
346 January. These constraints reduced the realm of possible monthly dormancy periods for the  
347 species to either 18 or 22 options (e.g., five months duration beginning in September, six  
348 months duration beginning in October, etc.). We treated these options as hypotheses and  
349 tested them by fitting simple linear models to pixel-wise seasonal abundance data, assuming  
350 diapause periods and feeding seasons to differ in mean copepod abundance in the surface  
351 layer. The most probable dormant period was assumed to be the one for which the  
352 corresponding model had the lowest Akaike information criterion (AIC) value. Once the most  
353 probable diapause period was identified, the abundance of hibernating copepods was  
354 estimated: we assumed a staggered onset of seasonal migration with individuals of a number

355 equivalent to the current surface-layer population descending during each of the last three  
356 feeding season months.

### 357 *Correlations in changes of decadal trends*

358 We used two-sided correlation tests to estimate strength and significance of  
359 correlations between decadal changes in carbon fluxes and changes in variables feeding into  
360 the carbon flux models, including sea surface temperature, community mean equivalent  
361 spherical radius, copepod biomass, copepod abundance, and abundance of important copepod  
362 taxa. Changes were estimated pixel-wise on a  $1^\circ \times 1^\circ$  grid and between all consecutive  
363 periods. Pearson correlation tests were used when both variables tested were interpolated  
364 with the same error distribution, otherwise Spearman correlation tests were used.

### 365 **Mechanistic models**

#### 366 *Modelling fecal pellet and DVM fluxes*

367 Estimates of fecal pellet fluxes and DVM fluxes were based on a recently published  
368 optimal behavior model<sup>7</sup> that we complemented with three major aspects: we considered the  
369 effects of temperature through temperature-dependent formulations of metabolic rates; we  
370 forced DVM duration to match empirical estimates at the community level; and we also  
371 modeled carbon export through fecal pellets during the time copepods spend feeding at the  
372 surface.

#### 373 *Optimal migration behavior model*

374 The model<sup>7</sup> assumes a copepod faces a common trade-off between acquiring energy  
375 for growth and reproduction and avoiding predation. This trade-off can be formalized by

376 Gilliam's rule<sup>41</sup> which defines optimal behavior as that which maximizes net energy gain  
 377 divided by mortality rate. In the context of DVM, the optimal behavior may be defined as a  
 378 function of the depth of migration ( $z_{max}$ ) and the fraction of day spent migrating ( $\tau$ ):

$$379 \quad f(z_{max}, \tau) = \frac{\varepsilon_{assim}g(z_{max}, \tau) - c(z_{max}, \tau)}{\mu(z_{max}, \tau)} \quad (3)$$

380 where  $g$  is the total energy consumed ( $J d^{-1}$ ) and  $\varepsilon_{assim}$  the assimilation efficiency: we  
 381 assume that the food consumed by copepods is channeled to equal parts into catabolic  
 382 metabolism (growth) ( $\varepsilon_{gr}$ ), anabolic metabolism ( $\varepsilon_{resp}$ ) where it is ultimately respired, and into  
 383 defecation ( $\varepsilon_{fec}$ ). The assimilation efficiency is the sum of the former two channels ( $\varepsilon_{assim} =$   
 384  $\varepsilon_{gr} + \varepsilon_{resp} = 2/3$ ).  $c$  is the energetic cost of the behavior ( $J d^{-1}$ ) and  $\mu$  is the mortality rate  
 385 ( $d^{-1}$ ). We define the total energy gain ( $g$ ) as a function of the amount of food taken up divided  
 386 by the relative metabolic day length

$$387 \quad g(z_{max}, \tau) = \beta e_p (1 - \tau) \times \frac{1}{d_m(z_{max}, \tau)} \quad (4)$$

388 where the coefficient  $e_p$  is the energy content of the prey ( $J gC^{-1}$ ),  $1 - \tau$  is the fraction of  
 389 the day spent feeding, and  $\beta$  is the feeding rate ( $gC d^{-1}$ ). We assume that feeding rate depends  
 390 on body mass and temperature and has a linear relationship with food availability up to a  
 391 threshold defined by maximum ingestion rate

$$392 \quad \beta = \min(a_c(m_c)m_c c_p Q_{10}^{\frac{(15-T_{z0})}{10}}, a_i(m_c)m_c Q_{10}^{\frac{(15-T_{z0})}{10}}) \quad (5)$$

393 where  $a_c(m_c)$  and  $a_i(m_c)$  are empirical, mass-dependent estimates of mass-specific  
 394 clearance rate and maximum ingestion rate, respectively, at a reference temperature<sup>31</sup> of 15  
 395 °C.  $m_c$  is copepod body mass ( $g C$ ), and  $c_p$  is the available phytoplankton biomass ( $g m^{-3}$ ).

396 The parameter  $Q_{10}$  is the factor by which metabolic rates change for a temperature change of  
 397 10 °C, which we assumed to be 2.8. Finally,  $T_{z0}$  is the temperature at grazing depth

398 (°C).where  $a_c(m_c)$  and  $a_i(m_c)$  are empirical, mass-dependent estimates of mass-specific  
 399 clearance rate and maximum ingestion rate, respectively, at a reference temperature<sup>31</sup> of 15  
 400 °C.  $m_c$  is copepod body mass (g C), and  $c_p$  is the available phytoplankton biomass (g m<sup>-3</sup>).  
 401 The parameter  $Q_{10}$  is the factor by which metabolic rates change for a temperature change of  
 402 10 °C, which we assumed to be 2.8. Finally,  $T_{z0}$  is the temperature at grazing depth (°C).

403 The relative metabolic day length ( $d_m$ ) in equation (4) is estimated as the base  
 404 metabolic activity experienced when migrating to deeper, cooler layers relative to the  
 405 expected base activity when staying at the surface:

$$406 \quad d_m(z_{max}, \tau) = (1 - \tau) + \tau Q_{10}^{-(T_{zmax}-T_{z0})/10} \quad (6)$$

407 whereby  $T_{zmax}$  is the temperature at migration depth (°C). By considering the  
 408 metabolic day length, resting phases at cool temperatures are rewarded, as they allow a more  
 409 efficient consumption of the energy taken-up.

410 The other two terms needed to estimate optimal migration behavior (Eq. 3) are  
 411 mortality ( $\mu$ ) and cost ( $c$ ). Many pelagic predators, for example fish, use visual cues to detect  
 412 their prey, and we therefore assume predation mortality to depend on light exposure. Light  
 413 exposure changes with migration depth, but also with water turbidity, time of the day, season  
 414 and latitude. We approximated local turbidity with remotely sensed estimates of the  
 415 extinction coefficient of irradiance at 490 nm wave length (KD490) and assumed an elevated  
 416 mortality factor of 50 to obtain realistic migration depths<sup>10</sup> (see ref. <sup>7</sup> for details).

417 The cost of migrating arises from the energy demands for swimming. Swimming costs  
 418 depend on the size of the copepods - as large organisms are more efficient swimmers than

419 small organisms – and they are proportional to the squared swimming velocity which  
420 depends on the migration depth (see ref. <sup>7</sup> for details).

#### 421 *Determining the optimal migration behavior*

422 The frame-work formulated above provides a strong mechanistic reasoning for size-  
423 dependent differences in DVM behavior of different individuals. However, the assumption  
424 that predation risk is only a function light intensity ignores spatiotemporal variations imposed  
425 by factors like predator abundance, which are more difficult to quantify. In order to still  
426 account for such spatiotemporal variations, we forced modeled behaviors to match our  
427 empirical estimates of DVM duration on the community level. To this end we fixed average  
428 DVM duration when we sample-wise optimized for the migration durations and depths of the  
429 observed taxa which yield the highest mass-weighted mean fitness. A detailed description of  
430 the optimization procedure is given in the Supplementary Methods.

#### 431 *Carbon export from fecal pellets*

432 We assumed that fecal pellets are produced in response to feeding with a delay of 30  
433 min gut transit time<sup>42</sup>. We estimated the fecal pellet fluxes individually for each taxon in a  
434 sample as the amount of pellets produced that did not remineralize before they have reached  
435 the vertical boundary (mixed layer depth or 500 meters depth),

$$436 \quad Flux_{fecal,i} = \frac{FPCP_i}{RR+SR_i/h} \frac{\tau_{opt,i}-t_t}{\tau_{opt,i}} e^{(-RR/SR_i)(z_0-z_b)} SR_i n_i \quad (7)$$

437 where  $z_b$  is the depth of the vertical boundary and  $z_0$  is grazing depth.  $SR_i$  (m d<sup>-1</sup>) is the  
438 fecal pellet sinking rate which depends on fecal pellet volume and ultimately copepod  
439 prosome length<sup>4</sup>. We assume that  $SR$  decreases with depth as remineralization continuously  
440 reduces the volumes of the pellets.  $RR$  represents specific remineralization rate (d<sup>-1</sup>) which we

441 assumed to be temperature-dependent.  $h$  is the thickness of the surface layer;  $t_t$  represents gut  
 442 transit time; and  $n$  is the abundance of the observed taxon  $i$ .  $FPCP_i$  is the fecal pellet carbon  
 443 production ( $\text{gC m}^3 \text{d}^{-1}$ ) estimated as

$$444 \quad FPCP_i = g(z_{max,opt,i}, \tau_{opt,i}) d_m(z_{max,opt,i}, \tau_{opt,i}) \varepsilon_{fec} \frac{1}{e_p} \quad (8)$$

445 with  $g$  being the energy gain at optimal migration behavior,  $d_m$  the relative metabolic day  
 446 length,  $1/e_p$  the energy to carbon ratio, and  $\varepsilon_{fec}$  the defecated fraction of the carbon consumed.  
 447 A description of the depth-dependent calculation of remineralization loss is given in the  
 448 Supplementary Methods.

#### 449 *Carbon export from daily vertical migration*

450 We define the carbon export through daily vertical migration as the fraction of daily  
 451 respiration that happens below the mixed layer plus one stomach volume of fecal pellets  
 452 released at migration depth:

$$453 \quad Flux_{resp,i} =$$

$$454 \quad g(z_{max,opt,i}, \tau_{opt,i}) \frac{1}{e_p} \varepsilon_{resp} \tau_{ML,i} Q_{10}^{-(T_{zmax}-T_{z0})/10} n_i h +$$

$$455 \quad \frac{FPCP_i}{RR+SR_i/h} \frac{t_t}{\tau_{opt,i}} e^{(-RR/SR_i)(z_{max,opt,i}-MLD)} SR_i n_i \quad (9)$$

456 Here,  $g$  is the energy gain from the optimal behavior;  $1/e_p$  the energy to carbon ratio;  
 457  $\varepsilon_{resp}$  is the respired fraction; and  $\tau_{ML,i}$  is the fraction of day spent below the mixed layer. The  
 458  $Q_{10}$ -term describes the relative reduction of respiration due to the temperature difference at  
 459 depth analogously to Eq. 6;  $n$  represents the abundance of individuals of taxon  $i$ ; and  $h$  is the  
 460 thickness of the representative surface layer. The second term is analogous to the fecal pellet  
 461 flux, except that remineralization loss only takes place from the maximum migration depth to

462 *MLD*, and that the excreted amount only corresponds to one stomach volume, which we  
 463 estimate as one gut transit time of grazing. An overview over the parameters and constants  
 464 used to estimate fecal pellet and DVM fluxes is given in Supplementary Table 2.

### 465 **Modelling hibernation fluxes**

466 We estimated carbon fluxes for each of hibernating species individually before  
 467 summing them up. Three main processes contribute to carbon fluxes through copepods in  
 468 diapause below the permanent thermocline: respiration, mortality and expiring females -  
 469 females which end their life cycles at depth in spring after having released their eggs<sup>14</sup>. Visser  
 470 et al. (ref. <sup>14</sup>) propose a general form to estimate these terms for dormant copepod species:

$$\begin{aligned}
 471 \quad Flux_{hiber,i} = & \sum_{stage} n_i \frac{(1-e^{-\mu_i D_i})}{\mu_i D_i} r_i D_i + \sum_{stage} n_i (1 - e^{-\mu_i D_i}) \left( m_i + w_{i,max} - \right. \\
 472 \quad & \left. \frac{r_i D_i}{2} \right) + \xi n_F e^{-\mu_F D_F} (m_F + w_{F,max} - r_F D_F - C_{egg}) \quad (10)
 \end{aligned}$$

473 where *stage* are the dormant life stages, *n* is abundance at the beginning of the  
 474 dormancy period, and *D* is the duration of the dormancy period.  $\mu$  is mortality, which we  
 475 assume to be 0.001 d<sup>-1</sup> (ref. <sup>14</sup>). *m* and *w* are structural and reserve mass, respectively, which  
 476 can be estimated based on their relationship with the prosome length (see ref. <sup>14</sup>). *r* is the  
 477 respiration rate which is a function of the body size of the dormant life stage, as well as the  
 478 local temperature (see ref. <sup>14</sup>) which we represented with temperature data at 500 m depth.  $\xi$   
 479 is the fraction of females that expire at depth, which is one for *Calanus hyperboreus* and zero  
 480 for *C. finmarchicus*, and *C. glacialis*. We assumed adult females to represent 25% of the  
 481 hibernating *Calanus* taxa sampled by the CPR, as these classes contain both copepodite V life  
 482 stages and adults, as well as both sexes. Finally, *C<sub>egg</sub>* is the amount of carbon invested in egg  
 483 production, assumed to be 900  $\mu$ gC.

484           **Availability**

485           **Data**

486           Data generated to support the findings of this study are available within the paper and  
487 its supplementary information files.

488           **Code**

489           All analyses were conducted in the R environment<sup>32</sup>. Maps were created with the  
490 software Generic Mapping Tools<sup>43</sup>. Code generated for analyses and mapping is available  
491 from the corresponding author upon reasonable request.



492

## References

- 493 1. Sigman, D. M. & Boyle, E. A. Glacial/interglacial variations in atmospheric carbon  
494 dioxide. *Nature* **407**, 859–869 (2000).
- 495 2. Sanders, R. *et al.* The Biological Carbon Pump in the North Atlantic. *Prog. Oceanogr.*  
496 **129**, 200–218 (2014).
- 497 3. Steinberg, D. K. & Landry, M. R. Zooplankton and the Ocean Carbon Cycle. *Ann.*  
498 *Rev. Mar. Sci.* **9**, 413–444 (2017).
- 499 4. Stamieszkin, K. *et al.* Size as the master trait in modeled copepod fecal pellet carbon  
500 flux. *Limnol. Oceanogr.* **60**, 2090–2107 (2015).
- 501 5. Turner, J. T. Zooplankton fecal pellets, marine snow, phytodetritus and the ocean's  
502 biological pump. *Prog. Oceanogr.* **130**, 205–248 (2015).
- 503 6. Hays, G. C. Zooplankton avoidance activity. *Nature* **376**, 650–650 (1994).
- 504 7. Hansen, A. N. & Visser, A. W. Carbon export by vertically migrating zooplankton: an  
505 optimal behavior model. *Limnol. Oceanogr.* **61**, 701–710 (2016).
- 506 8. Steinberg, D. K. *et al.* Zooplankton vertical migration and the active transport of  
507 dissolved organic and inorganic carbon in the Sargasso Sea. *Deep Sea Res. Part I*  
508 *Oceanogr. Res. Pap.* **47**, 137–158 (2000).
- 509 9. Al-Mutairi, H. & Landry, M. R. Active export of carbon and nitrogen at Station  
510 ALOHA by diel migrant zooplankton. *Deep Sea Res. Part II Top. Stud. Oceanogr.* **48**,  
511 2083–2103 (2001).

- 512 10. Ohman, M. D. & Romagnan, J.-B. Nonlinear effects of body size and optical  
513 attenuation on Diel Vertical Migration by zooplankton. *Limnol. Oceanogr.* **61**, 765–  
514 770 (2016).
- 515 11. Dahms, H. U. Dormancy in the Copepoda - an overview. *Hydrobiologia* **306**, 199–211  
516 (1995).
- 517 12. Brun, P., Payne, M. R. & Kiørboe, T. A trait database for marine copepods. *Earth Syst.*  
518 *Sci. Data* **9**, 99–113 (2017).
- 519 13. Jónasdóttir, S. H., Visser, A. W., Richardson, K. & Heath, M. R. Seasonal copepod  
520 lipid pump promotes carbon sequestration in the deep North Atlantic. *Proc. Natl.*  
521 *Acad. Sci. U. S. A.* **112**, 12122–6 (2015).
- 522 14. Visser, A. W., Grønning, J. & Jónasdóttir, S. H. Calanus hyperboreus and the lipid  
523 pump. *Limnol. Oceanogr.* **62**, 1155–1165 (2017).
- 524 15. Bradford-Grieve, J. M. Potential contribution that the copepod *Neocalanus tonsus*  
525 makes to downward carbon flux in the Southern Ocean. *J. Plankton Res.* **23**, 963–975  
526 (2001).
- 527 16. Richardson, A. J. *et al.* Using continuous plankton recorder data. *Prog. Oceanogr.* **68**,  
528 27–74 (2006).
- 529 17. Johns, D. G. Raw data for copepods in the North Atlantic (25-73N, 80W-20E) 1960-  
530 2014 as recorded by the Continuous Plankton recorder. (2016).  
531 doi:10.7487/2016.250.1.1007
- 532 18. Beaugrand, G., Edwards, M. & Legendre, L. Marine biodiversity, ecosystem

- 533 functioning, and carbon cycles. *Proc. Natl. Acad. Sci.* **107**, 10120–10124 (2010).
- 534 19. Sundby, S., Drinkwater, K. F. & Kjesbu, O. S. The North Atlantic Spring-Bloom  
535 System—Where the Changing Climate Meets the Winter Dark. *Front. Mar. Sci.* **3**,  
536 (2016).
- 537 20. Martinez, E., Antoine, D., D’Ortenzio, F. & de Boyer Montégut, C. Phytoplankton  
538 spring and fall blooms in the North Atlantic in the 1980s and 2000s. *J. Geophys. Res.*  
539 **116**, C11029 (2011).
- 540 21. Chivers, W. J., Walne, A. W. & Hays, G. C. Mismatch between marine plankton range  
541 movements and the velocity of climate change. *Nat. Commun.* **8**, 14434 (2017).
- 542 22. Poloczanska, E. S. *et al.* Global imprint of climate change on marine life. *Nat. Clim.*  
543 *Chang.* **3**, 919–925 (2013).
- 544 23. Edwards, M. & Richardson, A. J. Impact of climate change on marine pelagic  
545 phenology and trophic mismatch. *Nature* **430**, 881–4 (2004).
- 546 24. Greene, C. & Pershing, A. J. The response of *Calanus finmarchicus* populations to  
547 climate variability in the Northwest Atlantic: basin-scale forcing associated with the  
548 North Atlantic Oscillation. *ICES J. Mar. Sci.* **57**, 1536–1544 (2000).
- 549 25. Chust, G. *et al.* Are *Calanus* spp. shifting poleward in the North Atlantic? A habitat  
550 modelling approach. *ICES J. Mar. Sci.* **71**, 241–253 (2013).
- 551 26. Cermeño, P. *et al.* The role of nutricline depth in regulating the ocean. *Proc. Natl.*  
552 *Acad. Sci. U. S. A.* **105**, 20344–20349 (2008).

- 553 27. Palomares-Garcia, R. J., Gomez-Gutierrez, J. & Robinson, C. J. Winter and summer  
554 vertical distribution of epipelagic copepods in the Gulf of California. *J. Plankton Res.*  
555 **35**, 1009–1026 (2013).
- 556 28. Guidi, L. *et al.* Plankton networks driving carbon export in the oligotrophic ocean.  
557 *Nature* **532**, 465–470 (2016).
- 558 29. Boyd, P. W. Toward quantifying the response of the oceans' biological pump to  
559 climate change. *Front. Mar. Sci.* **2**, 1–15 (2015).
- 560 30. Intergovernmental Panel on Climate Change. in *Climate Change 2014 Impacts,*  
561 *Adaptation, and Vulnerability* (eds. Field, C. B., Barros, V. R., Dokken, D. J., Mach,  
562 K. J. & Mastrandrea, M. D.) 411–484 (Cambridge University Press, 2014).  
563 doi:10.1017/CBO9781107415379.011
- 564 31. Kiørboe, T. & Hirst, A. G. Shifts in Mass Scaling of Respiration, Feeding, and Growth  
565 Rates across Life-Form Transitions in Marine Pelagic Organisms. *Am. Nat.* **183**,  
566 E118–E130 (2014).
- 567 32. R Core Team. R: A Language and Environment for Statistical Computing. (2013).
- 568 33. Locarini, R. A. *et al.* *World Ocean Atlas 2013, Volume 1: Temperature.* (NOAA Atlas  
569 NESDIS 73, 2013).
- 570 34. Rayner, N. A. *et al.* Global analyses of sea surface temperature, sea ice, and night  
571 marine air temperature since the late nineteenth century. *J. Geophys. Res.* **108**, 4407  
572 (2003).
- 573 35. Kostadinov, T. S., Milutinović, S., Marinov, I. & Cabré, A. Carbon-based

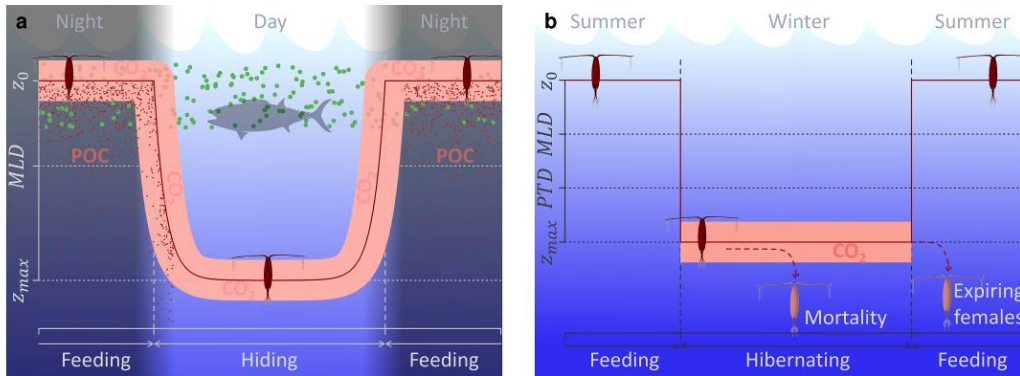
- 574 phytoplankton size classes retrieved via ocean color estimates of the particle size  
575 distribution. *Ocean Sci.* **12**, 561–575 (2016).
- 576 36. Schmidtko, S., Johnson, G. C. & Lyman, J. M. MIMOC: A global monthly isopycnal  
577 upper-ocean climatology with mixed layers. *J. Geophys. Res. Ocean.* **118**, 1658–1672  
578 (2013).
- 579 37. Amante, C. & Eakins, B. W. *ETOPO1 1 Arc-Minute Global Relief Model: Procedures,*  
580 *Data Sources and Analysis.* (NOAA Technical Memorandum NESDIS NGDC-24,  
581 National Geophysical Data Center, 2009). doi:10.7289/V5C8276M
- 582 38. Jiang, H. & Kiorboe, T. The fluid dynamics of swimming by jumping in copepods. *J.*  
583 *R. Soc. Interface* **8**, 1090–1103 (2011).
- 584 39. Rue, H., Martino, S. & Chopin, N. Approximate Bayesian inference for latent  
585 Gaussian models by using integrated nested Laplace approximations. *J. R. Stat. Soc.*  
586 *Ser. B (Statistical Methodol.* **71**, 319–392 (2009).
- 587 40. Blangiardo, M. & Cameletti, M. *Spatial and Spatio-temporal Bayesian Models with R-*  
588 *INLA.* (Wiley, 2015).
- 589 41. Gilliam, J. F. & Fraser, D. F. Habitat Selection Under Predation Hazard: Test of a  
590 Model with Foraging Minnows. *Ecology* **68**, 1856–1862 (1987).
- 591 42. Kiørboe, T. & Tiselius, P. T. Gut clearance and pigment destruction in a herbivorous  
592 copepod, *Acartia tonsa*, and the determination of in situ grazing rates. *J. Plankton Res.*  
593 **9**, 525–534 (1987).
- 594 43. Wessel, P., Smith, W. H. F., Scharroo, R., Luis, J. & Wobbe, F. Generic Mapping

595 Tools: Improved Version Released. *Eos, Trans. Am. Geophys. Union* **94**, 409–410  
596 (2013).

597

## Figures

598



599

Figure 1: Schematic illustrations of daily and annual vertical distributions of copepods

600

and associated carbon fluxes. Panel (a) shows carbon fluxes related to the daily vertical

601

migration behavior (fecal pellet flux and DVM flux). Panel (b) illustrates seasonal

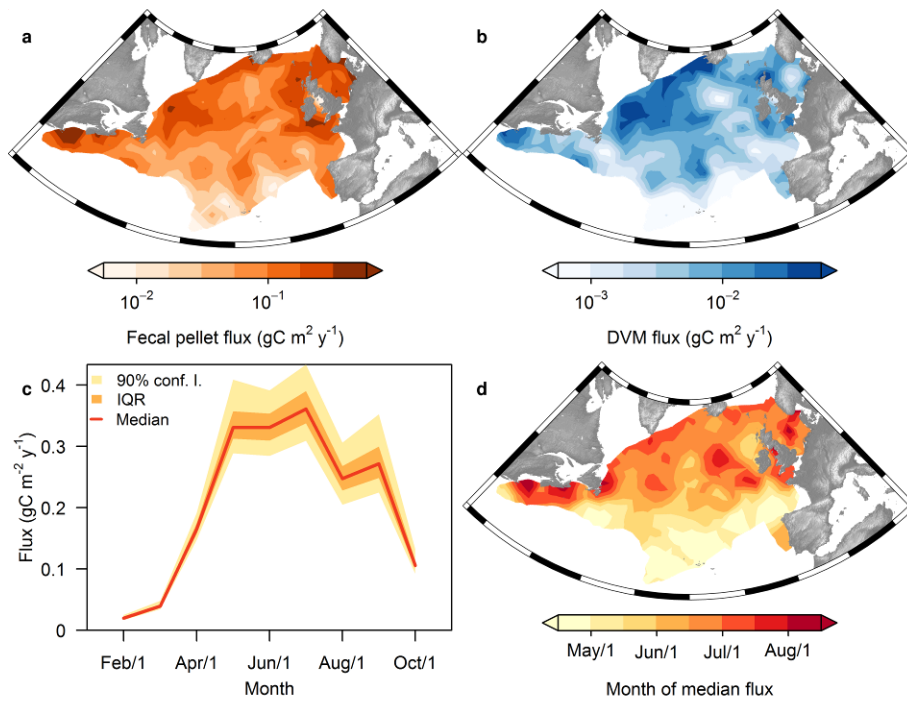
602

hibernation below the permanent thermocline (PTD) and associated hibernation flux. MLD

603

indicates mixed layer depth; POC represents particulate organic carbon.

604



605

606

Figure 2: Distribution and phenology of fecal pellet and DVM fluxes at mixed layer

607

depth for the period 2004-2014. Distributions of annual averages are shown for fecal pellet

608

(a) and DVM fluxes (b). Monthly averages of their sum are shown in panel (c) where the red

609

line connects medians and orange and yellow polygons illustrate interquartile range and 90%-

610

confidence intervals, respectively. Panel (d) shows the distribution of the timing of 50%

611

annual flux. Estimates for November and January are lacking due to missing information on

612

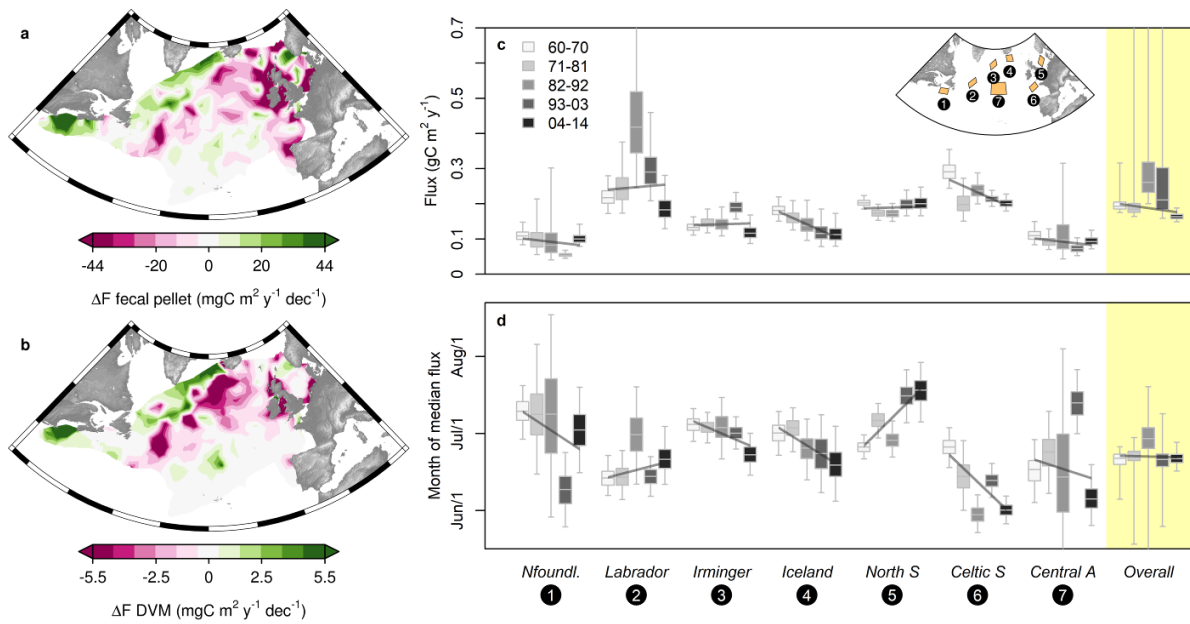
food availability (considered zero for averaging). Maps of interpolation uncertainty are

613

shown in Supplementary Figure 8.

614

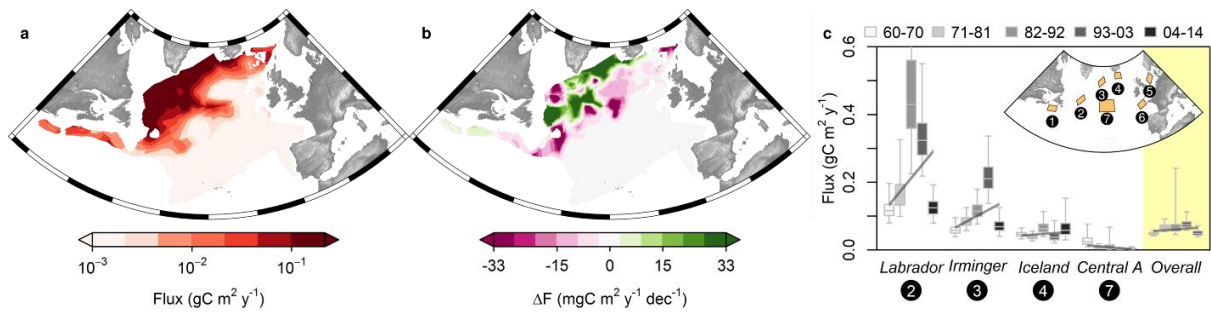




615

616 Figure 3: Trends in fecal pellet and DVM fluxes at mixed layer depth from 1960 to  
 617 2014. Slopes of linear regressions between flux estimates and time are shown for fecal pellet  
 618 fluxes (a) and DVM fluxes (b) at mixed layer depth. Decadal estimates of annual flux (c) and  
 619 timing of 50% annual flux (d) are shown with uncertainty from spatiotemporal interpolations  
 620 for the entire study area and seven focal areas. Central lines in boxplots illustrate medians,  
 621 boxes illustrate interquartile ranges and whiskers represent 95%-confidence intervals.  
 622 Superimposed trend lines illustrate changes in medians.

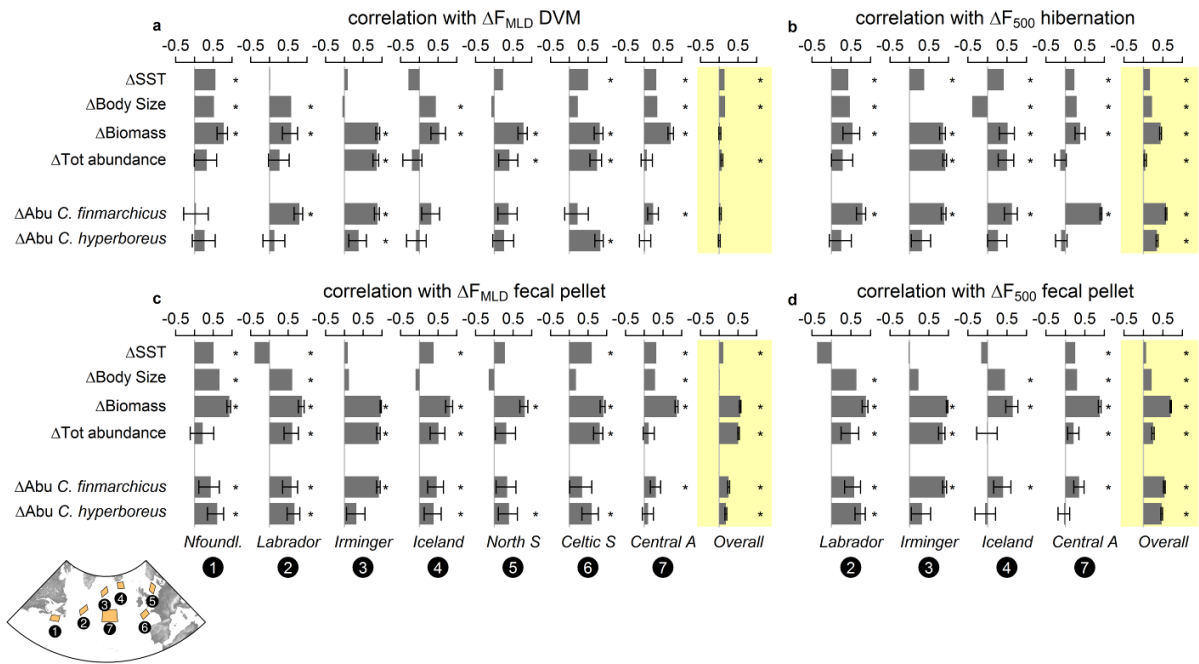
623



624

625 Figure 4: Distribution and trends in hibernation fluxes. Distributions for the period  
 626 2004-2014 are shown in panel (a). Slopes of linear regressions between flux estimates and  
 627 time are shown for the period 1960 to 2014 in panel (b). For focal areas deeper than 500m  
 628 periodical estimates are shown with uncertainty (c). Central lines in boxplots illustrate  
 629 medians, boxes illustrate interquartile ranges and whiskers represent 95%-confidence  
 630 intervals. Superimposed trend lines illustrate changes in medians.

631



632

633

Figure 5: Correlation coefficients between flux changes and changes in key variables

634

feeding into the models. Depicted are relationships of DVM flux at mixed layer depth (a),

635

hibernation flux at 500 m (b), fecal pellet flux at mixed layer depth (c), and fecal pellet flux at

636

500 m (d), with sea surface temperature, body size, biomass, and abundance. Correlation

637

coefficients were estimated for the entire study area and seven focal areas. Error bars indicate

638

95%-confidence intervals and asterisks indicate significance at the  $p \leq 0.01$  level. For

639

correlations between carbon fluxes and sea surface temperature or body size we used

640

Spearman correlation, otherwise Pearson correlation. Correlations with abundance of

641

additional taxa are shown in Supplementary Results.

642

643 **Supplementary information**

644 Pdf files:

645 Supplementary Information

646 **Acknowledgements**

647 We acknowledge the Villum foundation for support to the Centre for Ocean Life.  
648 Further support was received from the Gordon & Betty Moore Foundation through award  
649 #5479' (TK and AVW), the NSF GRFP grant #DGE-1144205 (KS), and the European Union  
650 7th Framework Programme (FP7 2007–2013) through grant agreement number 308299  
651 (NACLIM) (MRP). Finally, we wish to thank the many current and retired scientists at  
652 SAHFOS whose efforts over the years helped to establish and maintain the Continuous  
653 Plankton Recorder survey, and Hans van Someren Gréve for the beautiful copepod  
654 illustration.

655 **Author contributions**

656 PB, KS, AWW, MRP and TK designed the study. KS developed the fecal pellet  
657 model. PL selected the taxa used and compiled the data. PB performed the analysis and  
658 prepared the manuscript with contributions and support from the other authors.

659 **Competing interests**

660 The authors declare no competing financial interests.

661

662

663

664

## Supplementary Information

---

665

*to the paper "Climate change has altered zooplankton-fuelled carbon*

666

*export in the North Atlantic"*

667

## Dimensions of copepod taxa considered

670 Supplementary Table 1: Taxa considered in this study as sampled by the Continuous Plankton Recorder and  
 671 their estimated dimensions, including prosome length ( $PL$ ), prosome width ( $PW$ ), aspect ratio ( $\eta = PW/PL$ ),  
 672 body volume ( $V$ ), equivalent spherical radius ( $r$ ), and carbon mass ( $m$ ).

CPR taxon	$PL$ (mm)	$PW$ (mm)	$\eta$	$V$ (mm <sup>3</sup> )	$r$ (mm)	$m$ (mg C)
<i>Oncaea</i> spp.	0.54**	0.19	0.35 <sup>§</sup>	0.01	0.13	0.01
<i>Oithona</i> spp.	0.79	0.27*	0.34*	0.03	0.19	0.01
<i>Acartia</i> spp. (unidentified)	1.00	0.33*	0.33*	0.06	0.24	0.03
<i>Mecynocera clausi</i>	1.01	0.36*	0.36*	0.07	0.25	0.03
<i>Isias clavipes</i>	1.03 <sup>¶</sup>	0.36	0.35 <sup>§</sup>	0.07	0.26	0.03
<i>Calocalanus</i> spp.	1.09	0.39*	0.36*	0.09	0.27	0.04
<i>Corycaeus</i> spp.	1.09	0.43*	0.39*	0.11	0.29	0.05
<i>Para-Pseudocalanus</i> spp.	1.39	0.44*	0.32*	0.14	0.32	0.06
<i>Clausocalanus</i> spp.	1.29	0.47*	0.36*	0.15	0.33	0.06
<i>Centropages hamatus</i>	1.39	0.52*	0.37*	0.20	0.36	0.08
<i>Scolecithricella</i> spp.	1.40	0.52*	0.37*	0.20	0.36	0.09
<i>Calanus</i> I-IV	1.65	0.50*	0.30*	0.22	0.37	0.09
<i>Centropages bradyi</i>	1.45 <sup>¶</sup>	0.54	0.37 <sup>‡</sup>	0.22	0.38	0.09
<i>Centropages</i> spp. (Unidentified)	1.51	0.56 <sup>††</sup>	0.37 <sup>††</sup>	0.25	0.39	0.11
<i>Temora longicornis</i>	1.30	0.62*	0.48*	0.26	0.40	0.11
<i>Metridia</i> I-IV	1.66	0.60*	0.36*	0.31	0.42	0.13
<i>Labidocera wollastoni</i>	1.73 <sup>¶</sup>	0.60	0.35 <sup>§</sup>	0.33	0.43	0.14
<i>Centropages typicus</i>	1.69	0.63*	0.37*	0.35	0.44	0.15
<i>Mesocalanus tenuicornis</i>	1.79	0.64*	0.36*	0.38	0.45	0.16
<i>Pleuromamma borealis</i>	1.99	0.73*	0.37*	0.56	0.51	0.23
<i>Pleuromamma gracilis</i>	1.99	0.73*	0.37*	0.56	0.51	0.23
<i>Nannocalanus minor</i>	2.00	0.74*	0.37*	0.57	0.52	0.23
<i>Calanoides carinatus</i>	2.40	0.75*	0.31*	0.71	0.55	0.28
<i>Metridia longa</i>	2.3*	0.83	0.36*	0.84	0.58	0.33
<i>Calanus helgolandicus</i>	2.80	0.81*	0.29 <sup>a</sup>	0.96	0.61	0.38
<i>Anomalocera patersoni</i>	2.55 <sup>¶¶</sup>	0.89	0.35 <sup>§</sup>	1.06	0.63	0.42
<i>Pleuromamma</i> V-VI (Trav)	2.56 <sup>††</sup>	0.94	0.37 <sup>§§</sup>	1.18	0.66	0.46
<i>Metridia</i> Total traverse	2.60 <sup>¶¶</sup>	0.94	0.36 <sup>¶¶</sup>	1.21	0.66	0.47
<i>Candacia armata</i>	2.60	1.00*	0.38*	1.36	0.69	0.53
<i>Calanus finmarchicus</i>	2.99	0.95*	0.32*	1.41	0.70	0.55
<i>Subeucalanus crassus</i>	3.12	0.95*	0.30*	1.47	0.71	0.57
<i>Paraeuchaeta hebes</i>	2.91	1.04*	0.36*	1.65	0.73	0.63
<i>Metridia lucens</i>	2.90	1.05*	0.36*	1.67	0.74	0.64
<i>Neocalanus gracilis</i>	3.21	1.07*	0.33*	1.92	0.77	0.73
<i>Euchirella rostrata</i>	3.01	1.14*	0.38*	2.05	0.79	0.78
<i>Heterorhabdus norvegicus</i>	2.99	1.15*	0.38*	2.07	0.79	0.79
<i>Calanus glacialis</i>	3.57 <sup>¶</sup>	1.08	0.30 <sup>†</sup>	2.18	0.80	0.83
<i>Pleuromamma abdominalis</i>	3.49	1.28*	0.37*	3.00	0.89	1.12
<i>Rhincalanus nasutus</i>	5.02	1.14*	0.23*	3.41	0.93	1.27
<i>Undeuchaeta plumosa</i>	3.71	1.33*	0.36*	3.44	0.94	1.27
<i>Euchaeta acuta</i>	3.81	1.36*	0.36*	3.69	0.96	1.36
<i>Pleuromamma robusta</i>	3.99	1.46*	0.37*	4.45	1.02	1.63
<i>Pleuromamma xiphias</i>	4.59	1.68*	0.37*	6.78	1.17	2.43
<i>Calanus hyperboreus</i>	6.40 <sup>¶</sup>	1.94	0.30 <sup>†</sup>	12.57	1.44	4.37
<i>Paraeuchaeta norvegica</i>	7.50	2.68*	0.36*	28.22	1.89	9.42

673 \* values obtained from refs. <sup>2</sup> and <sup>3</sup>; † average of corresponding values for *Calanus finmarchicus* and *Calanus helgolandicus*; ‡ average of  
674 corresponding values for *Centropages typicus* and *Centropages hamatus*; § average of corresponding values for all taxa considered; || values  
675 obtained from ref. <sup>4</sup>; ¶ values estimated as 0.75 x mean total length, as reported by ref. <sup>5</sup>; # value obtained from ref. <sup>6</sup>; \* Value obtained from  
676 <http://www.arcodiv.org/>; \*\* average of *Oncaea media*, *Oncaea mediterranea* and *Oncaea venusta* as obtained from ref. <sup>7</sup>; †† average of  
677 *Centropages* species considered. †† value obtained from ref. <sup>8</sup>. §§ average of *Pleuromamma* species considered. ||| Average of *Metridia* species  
678 considered.

## 679 **Spatiotemporal model design**

### 680 ***Average DVM duration***

681 The average duration of daily vertical migration was estimated based on the CPR  
682 observations and used to constrain the optimal behavior estimates (see below). We calculated  
683 a DVM index ( $DVM^*$ ) of the following form:

$$684 \quad DVM^* = \frac{bm_n - bm_d}{bm_n} \quad (S1)$$

685 where  $bm$  is mean biomass at night or day<sup>3</sup>. For each observation we first estimated  
686 biomass ( $\text{mgC m}^{-3}$ ) of the present copepods, and determined whether it was made at night or  
687 during daylight hours. Then, we interpolated  $bm_n$  and  $bm_d$  observations from the entire data  
688 set, using the ILNA approach with default priors and assuming zero-inflated, negative  
689 binomial error distributions. As  $DVM^*$  is based on the ratio between two interpolated fields  
690 with negative binomial error distributions, it is particularly susceptible to gaps in the  
691 observational data. We accounted for this vulnerability by interpolating on a coarse, discrete  
692 spatial mesh with 375 points (Supplementary Figure 1), and by simultaneously fitting  $bm_n$   
693 and  $bm_d$  using the spatiotemporal effect of the night-time observations as an additional,  
694 stabilizing predictor for the day-time observations. In a few locations (on average 3% of the  
695 area) the estimates of  $DVM^*$  went slightly below zero (i.e., more biomass during day time  
696 than at night). We treated these cases as sampling errors and set  $DVM^*$  to zero, i.e., assuming  
697 no migration. The average fraction of day spent migrating ( $\tau_c$ ) necessary for subsequent  
698 analyses was then estimated by multiplying  $DVM^*$  estimates with the local relative day  
699 length at the time of sampling.

700 ***Abundance, carbon fluxes, biomass, and equivalent spherical radius***

701 We modeled the spatial distribution of copepod abundance, carbon fluxes, copepod  
702 biomass, and mean equivalent spherical radius of copepods using default priors and a  
703 relatively fine spatial mesh with 1552 points (Supplementary Figure 1) and considered only  
704 observations made during night time (106,907 observations), when we assumed the entire  
705 community to be present. For fecal pellet and DVM fluxes the seasonal resolution did not  
706 include winter months (November to January) where satellite data on available phytoplankton  
707 biomass and water turbidity was not available for high latitudes (76,439 observations).  
708 Community-weighted mean equivalent spherical radius was estimated as the carbon mass-  
709 weighted mean of the radii of the taxa present<sup>11</sup>. We assumed zero-inflated, negative  
710 binomial error distributions for abundance, carbon fluxes and biomass, while normal  
711 distribution was assumed for the error of equivalent spherical radius estimates.

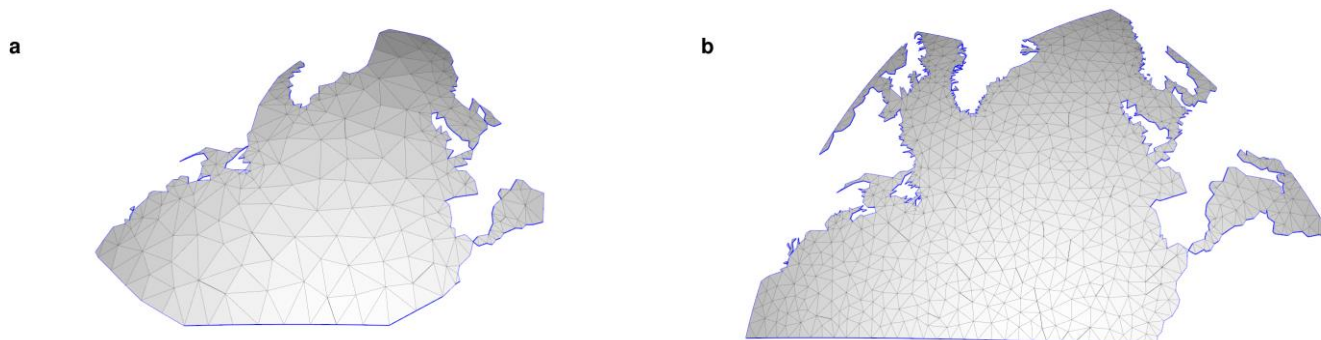
712 ***Uncertainty assessment***

713 One strength of estimating spatiotemporal interpolations with the INLA approach is  
714 that full uncertainty information is estimated. In the SPDE approach in INLA, for each mesh  
715 point (Supplementary Figure 1) not single values are provided but posterior probability  
716 distributions. The width of these probability distributions thereby depends on the number of  
717 local data points, their variability, and - if the standard deviation of the chosen error  
718 distribution family is a function of its mean - magnitude. These estimated probability  
719 densities allow the generation of replicate maps by resampling values for each mesh point  
720 and subsequent interpolation. We resampled 1000 such maps for uncertainty assessment, and  
721 used them to recalculate the quantities of interest. From these samples we derived uncertainty  
722 maps (Supplementary Figure 8) and estimated the regional medians and confidence intervals  
723 reported in the boxplots of Figs. 3c,d and 4c.



724

## Spatial meshes used in INLA



725

726 Supplementary Figure 1: Delaunay-triangulated mesh used to estimate the spatial dependencies in INLA  
 727 models. Panel (a) shows a crude mesh containing 375 vertices that is used to model daily vertical migration;  
 728 Panel (b) shows a fine mesh containing 1552 vertices that is to model carbon fluxes, biomass, abundance, and  
 729 body size (see Supplementary Methods). We projected the coordinates onto a sphere in order to realistically  
 730 represent the spatial relationships.

731

## Constants and parameters used to model fecal pellet and DVM fluxes

732 Supplementary Table 2: Overview over constants and parameters used to model fecal pellet and DVM fluxes

Parameter	Description	Value	Unit
$f$	Fitness		J
$g$	Gain from grazing		J d <sup>-1</sup>
$\mu$	Total mortality*		d <sup>-1</sup>
$c$	Cost of migration*		J d <sup>-1</sup>
$\tau$	Fraction of day spent migrating		-
$z_{max}$	Maximum migration depth		m
$z_0$	Grazing depth	7	m
$z_b$	Depth of the vertical boundary		m
$\epsilon_{assim}$	Assimilation efficiency	2/3	-
$\epsilon_{resp}$	Respired fraction of carbon intake	1/3	-
$\epsilon_{fec}$	Defecated fraction of carbon intake	1/3	-
$\epsilon_{gr}$	Carbon intake invested in growth	1/3	-
$e_p$	Energy content of prey	4200	J gC <sup>-1</sup>
$\beta$	Maximum feeding rate		m <sup>3</sup> d <sup>-1</sup>
$a_c(m_c)$	Specific clearance rate scaling at 15°C†		m <sup>3</sup> g C <sup>-1</sup> d <sup>-1</sup>
$a_i(m_c)$	Specific maximum ingestion rate scaling at 15°C†		g C g C <sup>-1</sup> d <sup>-1</sup>
$t_t$	Gut transit time	1/48	d
$d_m$	Relative metabolic day length		-
$Q_{10}$	Magnification of vital rates of active copepods at 10 °C increase	2.8	-
$FPCP$	Fecal pellet carbon production		gC m <sup>3</sup> d <sup>-1</sup>
$SR$	Fecal pellet sinking rate		m d <sup>-1</sup>
$RR$	Remineralization rate		d <sup>-1</sup>
$h$	Thickness of surface layer	14	m
$m_c$	Mass of copepod		g C
$r$	Radius of copepod		m

$T$	Temperature	°C
$n$	Copepod abundance	ind m <sup>-3</sup>
$c_p$	Available phytoplankton biomass	g m <sup>-3</sup>
$MLD$	Mixed layer depth	m

733 \* Parameter specified in ref. <sup>9</sup>; † Parameter specified in ref. <sup>10</sup>

## 734 **Optimizing daily vertical migration behaviors**

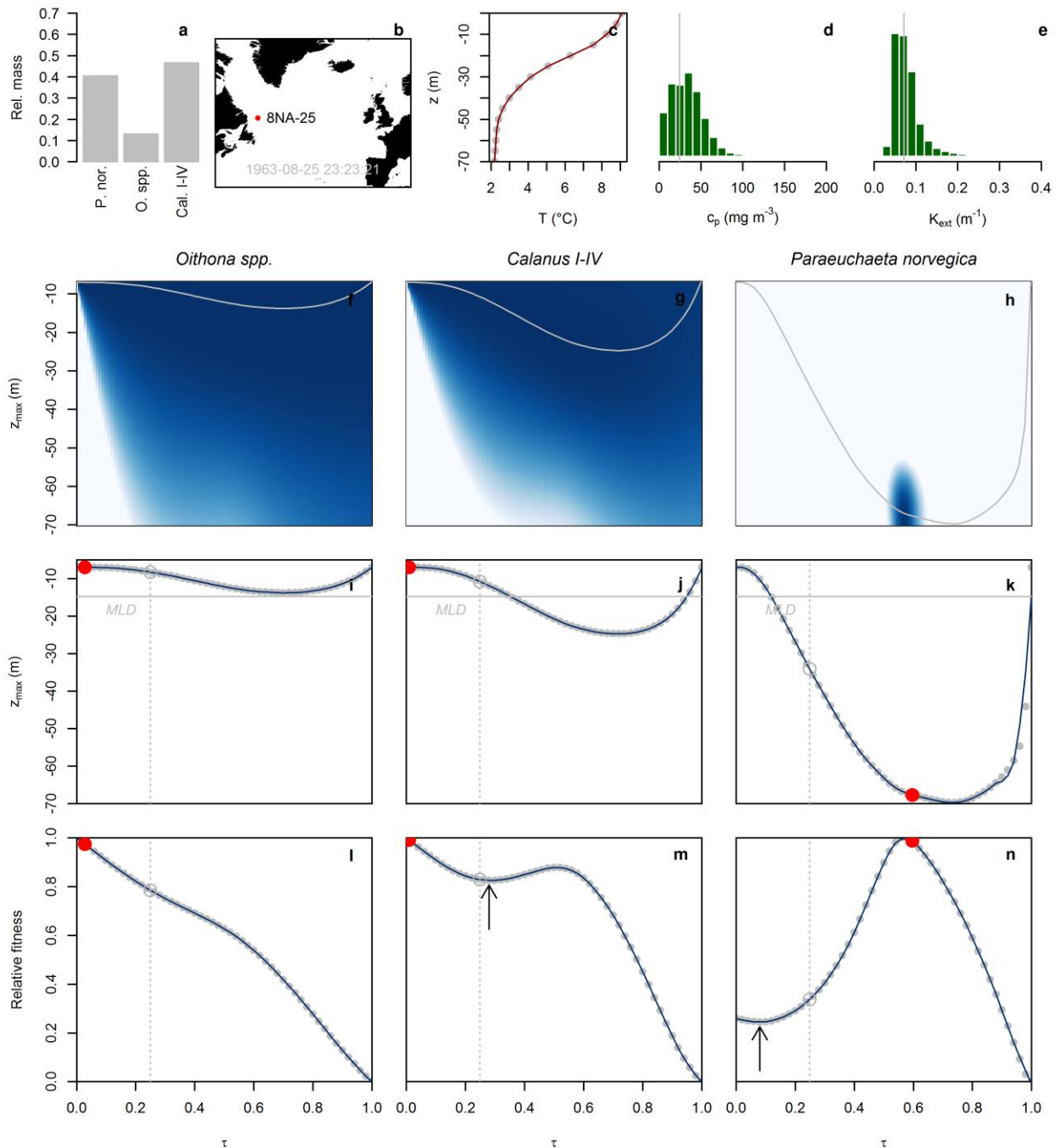
735 The optimization procedure employed consisted of two steps which will be illustrated  
736 at the example of CPR sample „8NA-25“ (Supplementary Figure 2). This sample was taken  
737 at the mouth of the Labrador Sea in August of 1963, and contained the taxa *Oithona* spp.,  
738 *Calanus* copepodites, and *Paraeuchaeta norvegica*. There was a significant thermal gradient  
739 in the top 70 meters, and roughly average food availability and water turbidity  
740 (Supplementary Figure 2a-e). In a first step we summarized the relative fitness for each taxon  
741 present and the given environmental conditions as a function of  $\tau$  and  $z_{max}$ . We discretized the  
742 range of  $\tau$  into 50 steps and derived optimal fitness and corresponding  $z_{max}$  for each of these  
743 steps, using the univariate Brent optimization algorithm<sup>12</sup>. Next, we interpolated between  
744 these optimum points to obtain functional relationships between  $\tau$  and optimal  $z_{max}$  as well as  
745 between  $\tau$  and optimal relative fitness using local polynomial regression fitting  
746 (Supplementary Figure 2i-n).

747 In a second step we used the functional relationships between  $\tau$  and optimal relative  
748 fitness to simultaneously determine the optimal migration behaviors of all taxa present in a  
749 sample. If more than one taxon was present in a sample we used the multidimensional  
750 Nelder-Mead optimization algorithm<sup>13</sup>, chose the observed average DVM duration (derived  
751 from the local  $DVM^*$  value) as starting point for each taxon, and maximized mean fitness  
752 under the constraint that mass-weighted mean DVM duration remains constant. In addition,  
753 we penalized high variance among the fitness estimates for the different taxa in order to avoid  
754 low fitness estimates for rare taxa. The optimization argument was thus

755 
$$\max\left(\frac{1}{\sum_i m_{c,i} n_i} \sum_i (f_i m_{c,i} n_i) - \text{var}(\mathbf{f})\right) \quad (\text{S2})$$

756 where  $m_{c,i}$  is the mass of taxon  $i$ ,  $n_i$  its abundance and  $\text{var}$  is variance, while  $f_i$  and  $\mathbf{f}$   
757 are relative fitness for taxon  $i$  and for all taxa present, respectively.

758 Three types of functional relationships between  $\tau$  and relative fitness were possible.  
759 Relative fitness could monotonously decrease with  $\tau$ , as in the exemplary case of small  
760 *Oithona* spp. sample „8NA-25“ (Supplementary Figure 2l) – the optimal behavior of the  
761 taxon is thus to remain at the surface; relative fitness could be highest at  $\tau=0$  and reach a local  
762 minimum around  $\tau=0.2$  and a local maximum around  $\tau=0.5$ , as in the exemplary case of  
763 intermediately-sized *Calanus* copepodites (Supplementary Figure 2m); or relative fitness  
764 could be highest around  $\tau=0.5$  and reach a local minimum close to  $\tau=0.2$ , as in the exemplary  
765 case of large *P. norvegica* (Supplementary Figure 2n). The local minima in the latter two  
766 cases could cause optimization problems if the starting values and the global maxima were on  
767 opposite sides of them, i.e., if the optimization had to go through a local minimum to reach a  
768 global maximum. If this was the case, and the constraint on  $\tau$  allowed for it, we adapted the  
769 starting values taxon-wise, and placed them in proximity of the global maxima. This  
770 adaptation was kept if it improved the optimization.



771

772           Supplementary Figure 2: Demonstration of optimization procedure at the example of CPR sample  
 773 „8NA-25“. Relative mass of taxa present is shown in panel (a); map with the location of the sample is shown in  
 774 panel (b); local temperature profile in the top 70 meters of the water column is shown in panel (c); available  
 775 phytoplankton carbon concentration at the sample site relative to the frequency distribution across the study area  
 776 shown in panel (d); light attenuation at the sample site relative to the frequency distribution across study area  
 777 is shown in panel (e); relative fitness of the taxa present as a function of migration duration ( $\tau$ ) and migration  
 778 depth ( $z_{max}$ ) is shown in panels (f-h). Superimposed grey lines indicate migration depths of maximum fitness as a  
 779 function of  $\tau$ . Relationships between  $\tau$  and  $z_{max}$  at optimal fitness and superimposed community optimization  
 780 results are shown in panels (i-k). Horizontal grey lines indicate local mixed layer depth. Relationships between  $\tau$   
 781 and optimal relative fitness with superimposed optimization results are shown in panels (l-n). In panels (i-n)  
 782 grey dots represent optimal fitness (l-n) and corresponding  $z_{max}$  (i-k) for a given value of  $\tau$ ; dark blue lines are

783 interpolations between these points using local polynomial regression fitting; dotted, vertical lines represent  
784 observed average migration duration (based on *DVM*\*) which is used as initial value in the community  
785 optimization, and red points indicate optimization results. Arrows in panels (m) and (n) highlight local minima  
786 which may pose challenges to the optimization algorithm.

## 787 **Remineralization rate**

788 A general relationship between fecal pellet remineralization and temperature has not  
789 been established yet and was therefore estimated based on available information from the  
790 literature. Carbon-specific degradation rates for diatom aggregates have been measured<sup>14</sup> at  
791  $12 \pm 3\%$  at 15 °C, while they were 3.5 times lower at 4 °C. Similarly, at warmer temperatures  
792 remineralization in the field has been shown to be confined to shallower layers<sup>15</sup>. Also, a  
793 study<sup>16</sup> conducted in the Sargasso Sea indicates a 75% reduction in the remineralization of  
794 organic material between 150 and 500 m. From these estimates, we designed a specific  
795 remineralization rate based on a linear relationship with temperature:

$$796 \quad RR = 0.005 T + 0.011 \quad (S3)$$

797 where  $T$  is temperature (°C). This relationship provided remineralization rates that  
798 decreased exponentially with depth, in line with estimates from particulate organic carbon  
799 profiles<sup>17,18</sup>.

## 800 **Depth-dependent remineralization loss**

801 Large fecal pellets sink faster than smaller pellets, and as pellets sink they lose  
802 volume through decomposition and remineralization. We explicitly modeled changes in both  
803 remineralization and fecal pellet sinking. To this end the depth range from the position of the  
804 copepod to the vertical boundary was divided into boxes that corresponded to the resolution  
805 of the temperature data (5-25 m). For each box the remineralization rate was estimated based  
806 on the local temperature. In addition, the local fecal pellet volume of each taxon present was

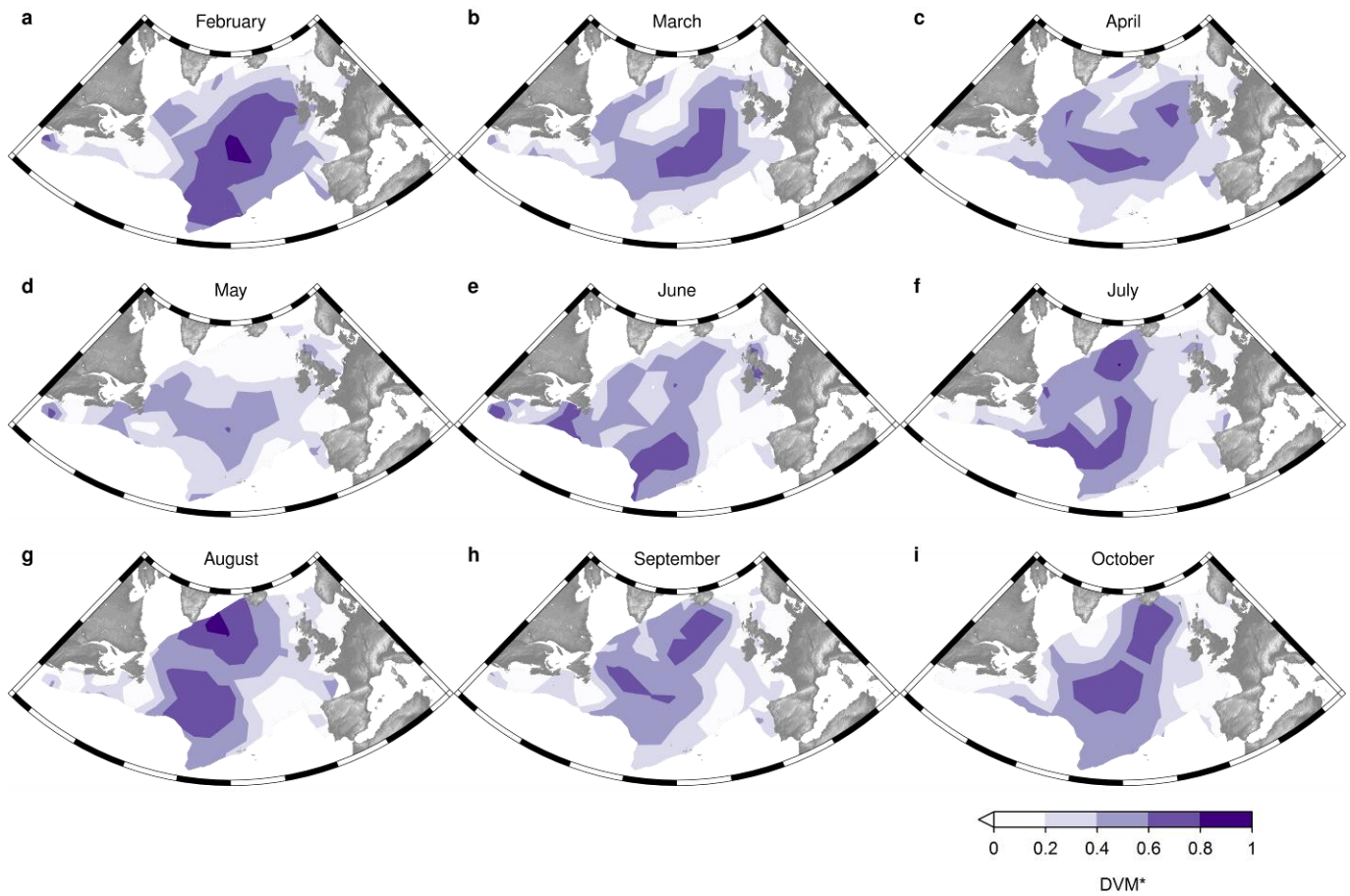
807 calculated by subtracting the volume lost while settling through the layers above from the  
808 initial volume. From the local fecal pellet volume a local sinking rate was calculated. Local  
809 remineralization rate and sinking rate were then used to calculate the remineralization loss  
810 through the box.

811

## Supplementary Results

812

### Observed fraction of the migrating biomass ( $DVM^*$ )



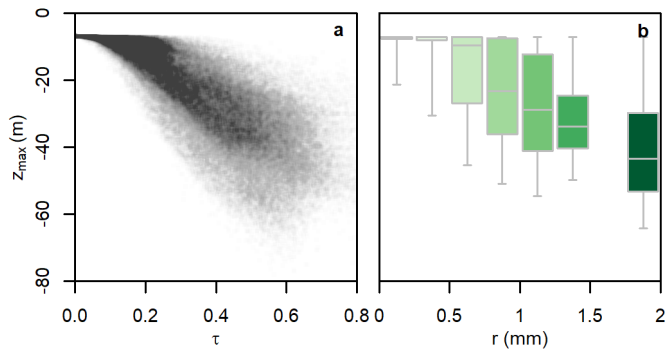
813

814 Supplementary Figure 3: Spatial distribution of the fraction of the migrating biomass ( $DVM^*$ ) estimated as the  
815 fraction of night-time biomass that disappears during day-light hours (see Methods for details). Average  $DVM^*$   
816 of the period 1960-2014 is shown for the months February to October (a-i).

817

818

## Identified optimal daily vertical migration behaviors



819

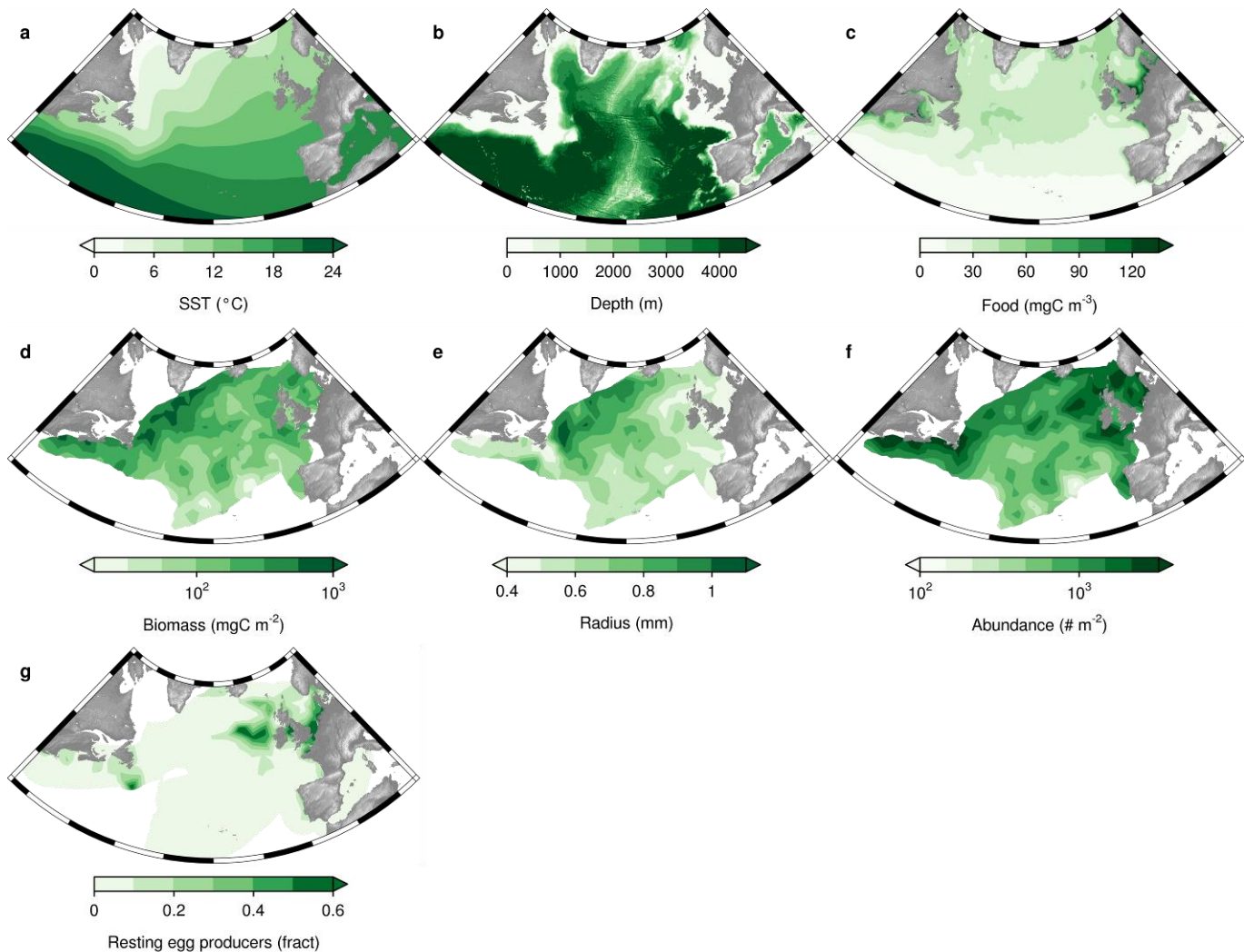
820 Supplementary Figure 4: Estimated values for migration depth ( $z_{max}$ ) depending on fraction of day spent  
821 migrating (a) and body size (b) for all taxa and observations.  $\tau$  represents fraction of day spent migrating and  $r$  is  
822 equivalent spherical radius of the organisms.

823



824

## Distribution of relevant variables



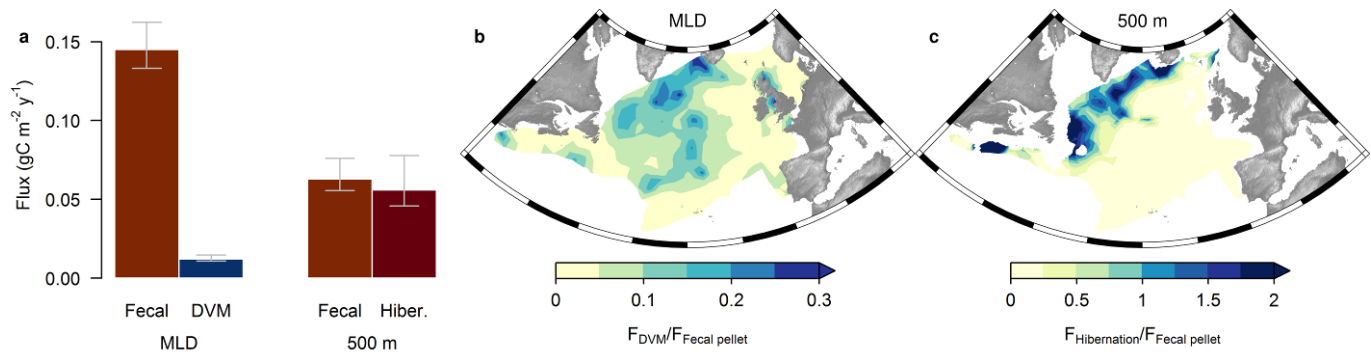
825

826 Supplementary Figure 5: Spatial distribution of variables with potential explanatory relevance. Illustrated are  
827 annual mean sea surface temperature (a), bathymetry (b), annual mean copepod food concentration (c), annual  
828 mean copepod biomass (d), annual mean prosome length (e), annual mean abundance (f), and annual mean of  
829 the weight fraction of resting egg producers (g). Distribution of weight fraction of resting egg producers is  
830 redrawn from ref. <sup>1</sup>.

831

832

## Relative importance of the different fluxes



833

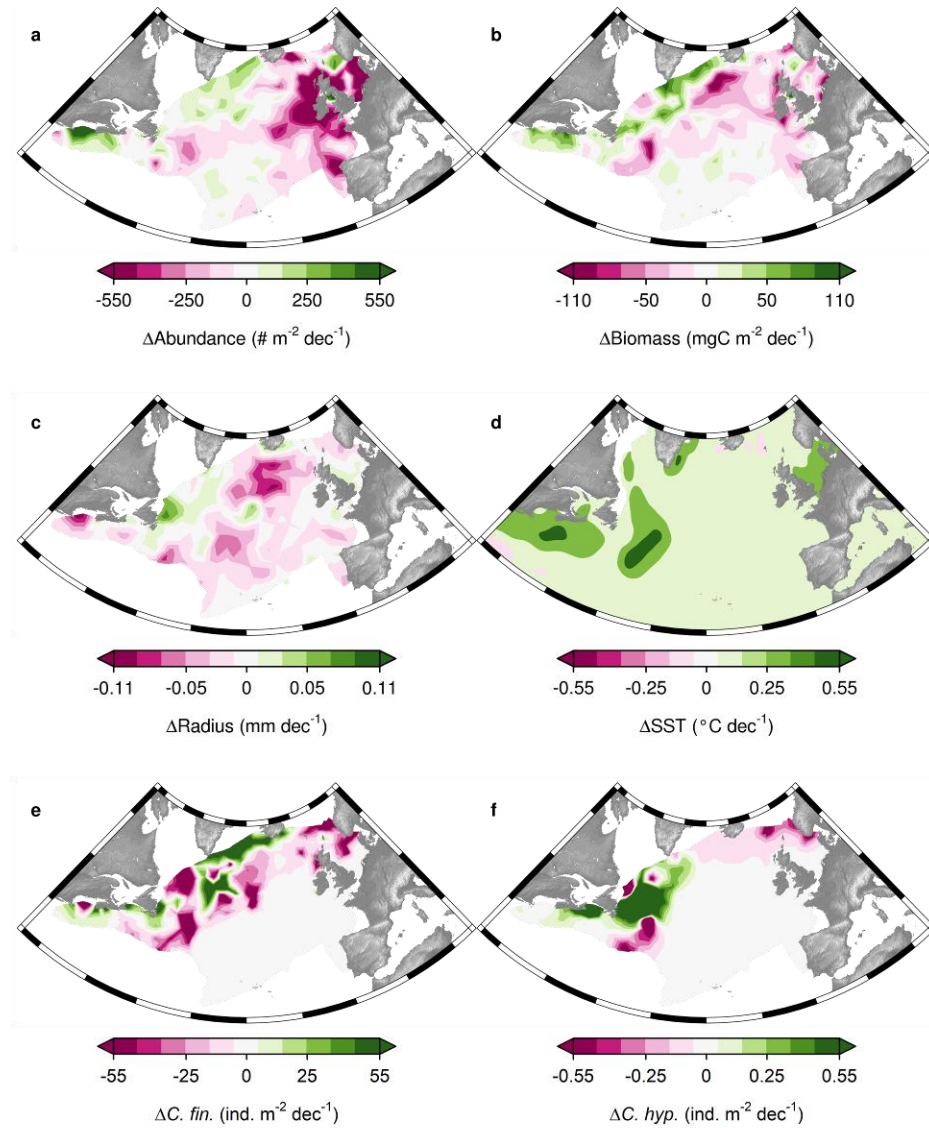
834 Supplementary Figure 6: Relative importance of the modeled carbon fluxes in the period 2004-2014. Total  
835 magnitude of fecal pellet and DVM fluxes at mixed layer depth and fecal pellet and hibernation fluxes at 500 m  
836 depth are shown in panel (a) where bars represent medians and error bars indicate 90% confidence intervals.  
837 Spatial distribution of ratios are shown for DVM and fecal pellet fluxes at mixed layer depth (b) and hibernation  
838 and fecal pellet fluxes at 500 m (c).

839

840

## Decadal changes of potential predictors

841

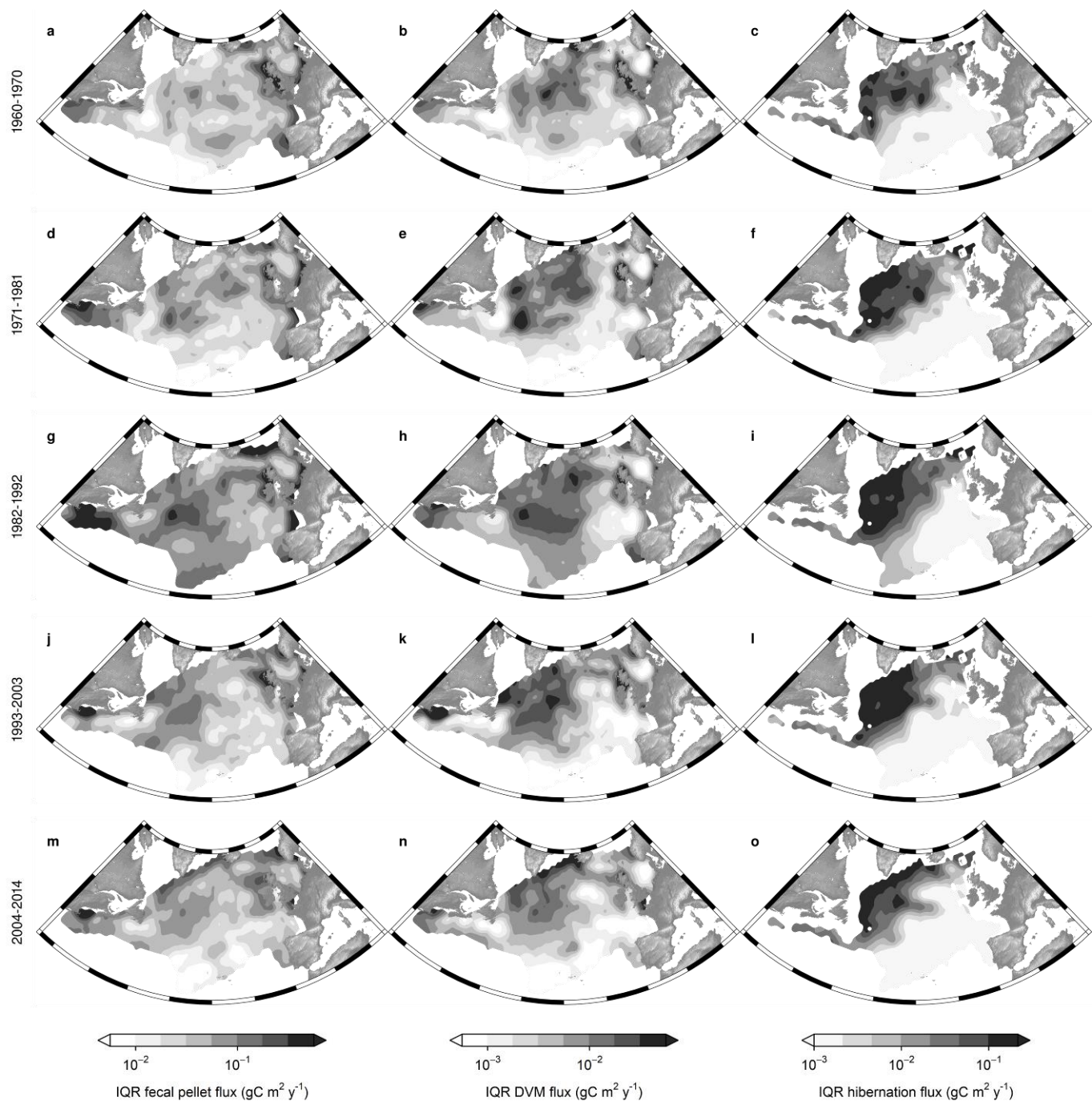


842

843 Supplementary Figure 7: Trends in potential predictors from 1960 to 2014. Illustrated are slopes of linear  
844 regressions between abundance (a), biomass (b), equivalent spherical radius (c), sea surface temperature (d),  
845 abundance of *C. finmarchicus* (e), abundance of *C. hyperboreus* (f), and time.

846

## Detailed uncertainty maps



849           Supplementary Figure 8: Uncertainty maps for fecal pellet and DVM fluxes at mixed layer depth and  
 850 for hibernation fluxes at 500 meters. Rows represent the periods considered. Uncertainty is represented as  
 851 interquartile ranges estimated from 1000-fold resampling of flux/abundance maps. Uncertainty depends on  
 852 sampling density, variability in observations, and mean abundance/flux, as for negative binomial distributions  
 853 variance is a function of the mean.

854

855

856

## Correlation coefficients between flux changes and abundance of further

857 **taxa**

858

859

860

861

862

Supplementary Table 3: Correlation coefficients between flux changes and changes in sea surface temperature, body size, biomass, and abundance of an extended set of abundant taxa for the entire study area. Changes were estimated pixel-wise on a  $1^\circ \times 1^\circ$  grid and between all subsequent periods. Subscripts indicate estimates at mixed layer depth or 500 meters. *Calanus* I-IV include pooled copepodite lifestages 1-4 of the four reported *Calanus* species. “Abu *Calanus* total” is the summed abundance of all reported *Calanus* classes.

	Corr. type	$\Delta F_{\text{MLD}}$ DVM	$\Delta F_{\text{MLD}}$ fecal pellet	$\Delta F_{500}$ fecal pellet	$\Delta F_{500}$ hibernation
$\Delta \text{SST}$	Spearman	0.15*	0.12*	0.09*	0.17*
$\Delta \text{Body size}$	Spearman	0.24*	0.07*	0.27*	0.22*
$\Delta \text{Biomass}$	Pearson	0.06*	0.6*	0.71*	0.44*
$\Delta \text{Tot abundance}$	Pearson	0.1*	0.48*	0.2*	0.05*
$\Delta \text{Abu C. finmarchicus}$	Pearson	0.07*	0.29*	0.51*	0.58*
$\Delta \text{Abu C. hyperboreus}$	Pearson	0	0.23*	0.5*	0.35*
$\Delta \text{Abu C. glacialis}$	Pearson	0.03*	0.05*	0.08*	0.37*
$\Delta \text{Abu C. helgolandicus}$	Pearson	0.05*	0.17*	0.07*	0.03
$\Delta \text{Abu Calanus I-IV}$	Pearson	-0.05*	0.16*	0.11*	0.07*
$\Delta \text{Abu Calanus total}$	Pearson	-0.01	0.26*	0.33*	0.32*
$\Delta \text{Abu Para-/Pseudocalanus}$	Pearson	0.12*	-0.05*	-0.11*	0.12*

863

\* correlation coefficient significantly different from zero,  $p \leq 0.01$

864

## Effect of surface-layer coprophagy on fecal pellet concentration

865

Among the abundant copepod taxa considered in this study *Oithona* spp. and *Oncaea*

866

spp. have been observed to include fecal pellets in their diet, thereby contributing to fecal

867

pellet flux attenuation in the epipelagic zone<sup>19–21</sup>. In a sensitivity analysis, we estimated the

868

magnitude and spatial distribution of the fraction of surface-layer fecal pellet concentration

869

potentially consumed by these organisms. To this end, we assumed the diet of *Oithona* and

870

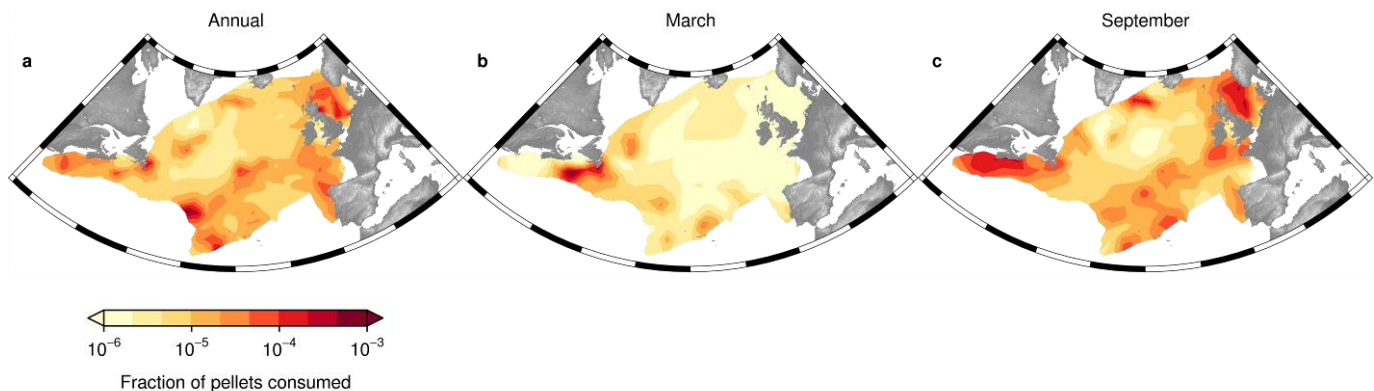
*Oncaea* to include both available phytoplankton biomass and fecal pellets of all studied

871

copepod taxa but themselves, and no preference between these food sources. The food

872 concentration available to these taxa was therefore somewhat elevated, increasing their  
873 feeding rates but also their own fecal pellet production.

874 For each observation we estimated the potential fraction of surface-layer fecal pellets  
875 removed by *Oithona* and *Oncaea* coprophagy and made spatiotemporal interpolations for the  
876 period 2004-2014 using the INLA approach with the same settings as we used to interpolate  
877 fecal pellet and DVM fluxes. The extent to which *Oithona* and *Oncaea* drew down surface-  
878 layer fecal pellet concentration ranged between 1-1000 ppm, i.e. 0.1 % at the most. Highest  
879 fractions were found in the southern central part of the study area where *Oncaea* regularly  
880 occurs<sup>22</sup>, as well as in the European and Northern American shelf seas, where *Oithona* is  
881 common<sup>22</sup>. In the areas of highest observed fecal pellet fluxes, the effect of surface-layer  
882 copepod coprophagy was generally lower.



883

884 Supplementary Figure 9: Fraction of fecal pellet carbon concentration consumed by coprophageous surface-  
885 layer copepods in the period 2004-2014. Spatial distribution of annual mean is shown in panel (a); estimates for  
886 March in panel (b); and estimates for September in panel (c).

## 887 **Relationship between recent NPP change and change in carbon fluxes**

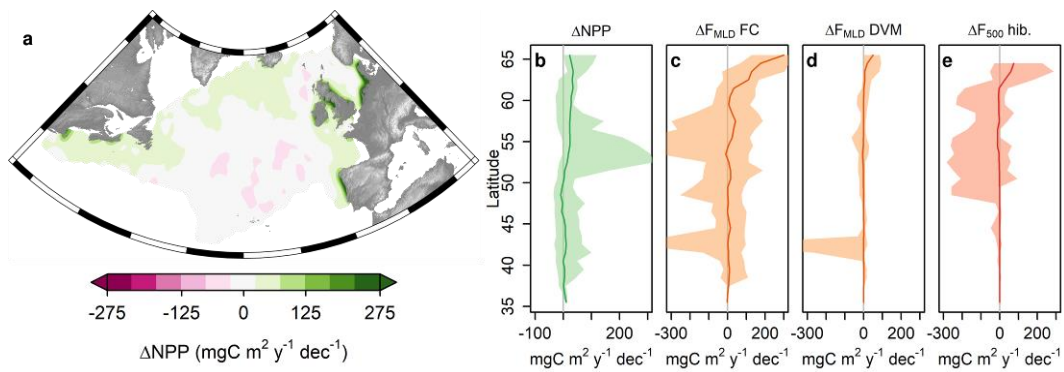
888 Spatially-resolved data on net primary productivity in the North Atlantic only exists  
889 since the launch of the Sea-Viewing Wide Field-of-View Sensor (SeaWiFS) program in late  
890 1997. We were therefore not able to fully compare how the temporal trends in carbon fluxes

891 through copepods matched changes in net primary productivity. However, by combining  
892 VGPM-algorithm-based estimates of NPP<sup>23</sup> from SeaWiFS and Moderate Resolution  
893 Imaging Spectroradiometer (MODIS) satellites  
894 ([www.science.oregonstate.edu/ocean.productivity/](http://www.science.oregonstate.edu/ocean.productivity/)), we could obtain at least a rough estimate  
895 of NPP change between the two most recent periods of carbon flux estimates.

896 For the periods 1997-2003 and 2004-2014 we estimated mean annual NPP and  
897 investigated how their difference relates to change in modeled carbon fluxes. For both  
898 periods we calculated annual means from the monthly estimates of March to November  
899 (remaining months were considered zero, as for fecal pellet and DVM flux estimates) and  
900 aggregated the data to 1°×1° horizontal resolution. Since no consistent NPP data set exists for  
901 the entire period, we estimated the first period from SeaWiFS-based NPP estimates and the  
902 second period from MODIS-based NPP estimates. We compared the consistency between the  
903 two data sets for the overlapping years 2004-2008. The distributions of annual means from  
904 these periods were very similar (Pearson correlation coefficient was 0.97) but MODIS-based  
905 NPP estimates were on average 5.6 mg C m<sup>-2</sup> y<sup>-1</sup> lower, for which we corrected before we  
906 calculated the difference between the two periods (Supplementary Figure 10a). In addition,  
907 we ran Spearman correlation tests between NPP changes and changes of mixed layer fecal  
908 pellet fluxes, mixed layer DVM fluxes and hibernation fluxes at 500 meters at the 1°×1°  
909 resolution. Note that this comparison is somewhat compromised by the mismatch in the first  
910 periods considered (1997-2003 for NPP and 1993-2003 for modeled carbon fluxes).

911 While NPP as well as modeled carbon fluxes mainly increased at higher latitudes  
912 during the last two decades, changes in space were only weakly related. NPP increased for  
913 the majority of pixels above about 53° North (Supplementary Figure 10a,b) while, carbon  
914 fluxes increased mainly above 60° North (Supplementary Figure 10c-e). The correlation

915 between changes in NPP and changes in fecal pellet flux was weakly positive (Spearman  
916 correlation  $r = 0.08$ ,  $p \leq 0.01$ ), the correlation with changes in DVM flux was non-significant  
917 ( $r = -0.06$ ,  $p > 0.01$ ), and the one with changes in hibernation flux was even slightly negative  
918 ( $r = -0.11$ ,  $p \leq 0.01$ ).



919

920 Supplementary Figure 10: Figure S2: NPP change between 1997-2003 and 2004-2014 and comparison to  
921 corresponding changes in modeled carbon fluxes. Spatial distribution of decadal changes in NPP (a) as well as  
922 medians (lines) and 90%-confidence intervals (polygons) of changes of NPP (b), mixed layer fecal pellet flux  
923 (c), mixed layer DVM flux (d) and hibernation flux at 500 meters (e) against latitude. Flux changes are shown  
924 between the periods 1993-2003 and 2004-2014.

925



926

## Supplementary Discussion

927

Here, we built a comprehensive framework that describes numerous processes

928

contributing to carbon fluxes mediated by surface-layer copepods. To be able to make

929

quantitative estimates, we had to simplify these processes and make limiting assumptions.

930

Furthermore, the observational data we used, although being perhaps the best of its kind, is

931

not a perfect reflection of the situation in the surface waters of the North Atlantic. Below we

932

discuss some major sources of uncertainty in our analysis related to data, feeding, and carbon

933

transport.

934

Our data underestimated the abundance of small copepods and ignored the

935

intraspecific variability of traits. The 270  $\mu\text{m}$  mesh of the Continuous Plankton Recorder

936

sampling device retains copepods with prosome lengths below one millimeter with reduced

937

efficiency<sup>24</sup>. While attempts have been made to correct for this<sup>25</sup>, finding a general way to do

938

so is difficult, because in areas of high abundance the mesh can clog and retain locally higher

939

fractions of small copepods. However, this limitation may have a restricted effect on flux

940

estimates as small individuals contribute proportionally less to carbon fluxes than the well-

941

sampled large ones. Besides not covering the entire community, the observations contain

942

variability induced by high population dynamics and water dispersal processes which could

943

make it difficult to robustly identify the duration of the feeding season of hibernating *Calanus*

944

species. Also our the trait data used had limitations: we had to rely on crude, taxon-wise

945

averages and empirical relationships, ignoring the sometimes significant intraspecific

946

variation<sup>4</sup>. In the future, observational data from *in-situ* imaging surveys<sup>26</sup> may resolve some

947

of these issues.

948           We had to make crude assumptions about the amount of the food consumed and the  
949 duration of the feeding period. By relying on size-resolved phytoplankton biomass  
950 estimates<sup>27</sup>, we employed a novel way to accurately estimate the amount of food available to  
951 copepods from remotely-sensed information. Still, we had no direct information on the  
952 amount of heterotrophic food, such as within sinking and suspended particles, as well as on  
953 food quality. Food quality influences feeding rates, digestion time, assimilation efficiency as  
954 well as structure and sinking properties of fecal pellets<sup>28</sup>. We further assumed that the feeding  
955 period was restricted to the time spent in the surface layer. Previous work in the field  
956 generally supports this assumption<sup>29,30</sup>, but these measurements are based on chlorophyll *a*  
957 fluorescence and may underestimate the contribution of heterotrophic prey.

958           Finally, there are uncertainties related to carbon transport in all modeled fluxes. Fecal  
959 pellets can undergo significant repackaging and fragmentation by zooplankton communities  
960 in deeper water layers<sup>28</sup>. This leads to the production of both small fragments and new,  
961 compact pellets impacting transport efficiency in ways that are poorly understood. Similarly,  
962 mortality during hibernation is an important but poorly understood process. We assumed it to  
963 be relatively low ( $0.001 \text{ d}^{-1}$ ) but small changes in this parameter can significantly impact  
964 carbon flux estimates<sup>31</sup>. In the case of daily vertical migration, migration depth is challenging  
965 to estimate, as both feeding loss and gain through lower mortality are weakly constrained.  
966 Since we assumed no feeding during migration, our feeding loss estimates may be rather  
967 high. In order to obtain realistic migration depths<sup>32</sup> we also assumed a high gain from reduced  
968 mortality (mortality factor<sup>9</sup> = 50).

969

970

## References

- 971 1. Holm, M. W. *et al.* Resting eggs in free living marine and estuarine copepods. *J.*  
972 *Plankton Res.* 1–14 (2017). doi:10.1093/plankt/fbx062
- 973 2. Hays, G. C., Proctor, C. A., John, A. W. G. & Warner, A. J. Interspecific differences in  
974 the diel vertical migration of marine copepods: The implications of size, color, and  
975 morphology. *Limnol. Oceanogr.* **39**, 1621–1629 (1994).
- 976 3. Hays, G. C. Large-scale patterns of diel vertical migration in the North Atlantic. *Deep*  
977 *Sea Res. Part I Oceanogr. Res. Pap.* **43**, 1601–1615 (1996).
- 978 4. Brun, P., Payne, M. R. & Kiørboe, T. A trait database for marine copepods. *Earth Syst.*  
979 *Sci. Data* **9**, 99–113 (2017).
- 980 5. Razouls, C., de Bovée, F., Kouwenberg, J. & Desreumaux, N. Diversity and  
981 Geographic Distribution of Marine Planktonic Copepods. Available at:  
982 <http://copepodes.obs-banyuls.fr/en>. (Accessed: 25th January 2016)
- 983 6. Halvorsen, E. Significance of lipid storage levels for reproductive output in the Arctic  
984 copepod *Calanus hyperboreus*. *Mar. Ecol. Prog. Ser.* **540**, 259–265 (2015).
- 985 7. Böttger-Schnack, R. & Schnack, D. Population structure and fecundity of the  
986 microcopepod *Oncaea bispinosa* in the Red Sea; a challenge to general concepts for  
987 the scaling of fecundity. *Mar. Ecol. Prog. Ser.* **302**, 159–175 (2005).
- 988 8. Richardson, A. J. *et al.* Using continuous plankton recorder data. *Prog. Oceanogr.* **68**,  
989 27–74 (2006).

- 990 9. Hansen, A. N. & Visser, A. W. Carbon export by vertically migrating zooplankton: an  
991 optimal behavior model. *Limnol. Oceanogr.* **61**, 701–710 (2016).
- 992 10. Kiørboe, T. & Hirst, A. G. Shifts in Mass Scaling of Respiration, Feeding, and Growth  
993 Rates across Life-Form Transitions in Marine Pelagic Organisms. *Am. Nat.* **183**,  
994 E118–E130 (2014).
- 995 11. Brun, P., Payne, M. R. & Kiørboe, T. Trait biogeography of marine copepods - an  
996 analysis across scales. *Ecol. Lett.* **19**, 1403–1413 (2016).
- 997 12. Brent, R. P. *Algorithms for Minimization without Derivatives*. (Prentice-Hall, 1973).
- 998 13. Nelder, J. A. & Mead, R. A Simplex Method for Function Minimization. *Comput. J.* **7**,  
999 308–313 (1965).
- 1000 14. Iversen, M. H. & Ploug, H. Temperature effects on carbon-specific respiration rate and  
1001 sinking velocity of diatom aggregates &ndash; potential implications for deep  
1002 ocean export processes. *Biogeosciences* **10**, 4073–4085 (2013).
- 1003 15. Marsay, C. M. *et al.* Attenuation of sinking particulate organic carbon flux through the  
1004 mesopelagic ocean. *Proc. Natl. Acad. Sci.* **112**, 1089–1094 (2015).
- 1005 16. McDonnell, A. M. P., Boyd, P. W. & Buesseler, K. O. Effects of sinking velocities and  
1006 microbial respiration rates on the attenuation of particulate carbon fluxes through the  
1007 mesopelagic zone. *Global Biogeochem. Cycles* **29**, 175–193 (2015).
- 1008 17. Martin, J. H., Knauer, G. A., Karl, D. M. & Broenkow, W. W. VERTEX: carbon  
1009 cycling in the northeast Pacific. *Deep Sea Res. Part A. Oceanogr. Res. Pap.* **34**, 267–  
1010 285 (1987).

- 1011 18. Boyd, P. W. & Trull, T. W. Understanding the export of biogenic particles in oceanic  
1012 waters: Is there consensus? *Prog. Oceanogr.* **72**, 276–312 (2007).
- 1013 19. Turner, J. T. Zooplankton fecal pellets, marine snow, phytodetritus and the ocean's  
1014 biological pump. *Prog. Oceanogr.* **130**, 205–248 (2015).
- 1015 20. Svensen, C. Is sedimentation of copepod faecal pellets determined by cyclopoids?  
1016 Evidence from enclosed ecosystems. *J. Plankton Res.* **25**, 917–926 (2003).
- 1017 21. Møller, E. F. *et al.* Production and fate of copepod fecal pellets across the Southern  
1018 Indian Ocean. *Mar. Biol.* **158**, 677–688 (2011).
- 1019 22. Barnard, R. *et al.* Continuous plankton records: Plankton Atlas of the north Atlantic  
1020 Ocean (1958-1999). II. Biogeographical charts. *Marine Ecology Progress Series* 11–  
1021 75 (2004).
- 1022 23. Behrenfeld, M. J. & Falkowski, P. G. Photosynthetic rates derived from satellite-based  
1023 chlorophyll concentration. *Limnol. Oceanogr.* **42**, 1–20 (1997).
- 1024 24. Hays, G. C. Mesh selection and filtration efficiency of the Continuous Plankton  
1025 Recorder. *J. Plankton Res.* **16**, 403–412 (1994).
- 1026 25. PITOIS, S. & FOX, C. Long-term changes in zooplankton biomass concentration and  
1027 mean size over the Northwest European shelf inferred from Continuous Plankton  
1028 Recorder data. *ICES J. Mar. Sci.* **63**, 785–798 (2006).
- 1029 26. Karsenti, E. *et al.* A Holistic Approach to Marine Eco-Systems Biology. *PLoS Biol.* **9**,  
1030 e1001177 (2011).

- 1031 27. Kostadinov, T. S., Milutinović, S., Marinov, I. & Cabré, A. Carbon-based  
1032 phytoplankton size classes retrieved via ocean color estimates of the particle size  
1033 distribution. *Ocean Sci.* **12**, 561–575 (2016).
- 1034 28. Steinberg, D. K. & Landry, M. R. Zooplankton and the Ocean Carbon Cycle. *Ann.*  
1035 *Rev. Mar. Sci.* **9**, 413–444 (2017).
- 1036 29. Dagg, M. J., Frost, B. W. & Newton, J. Diel vertical migration and feeding in adult  
1037 female *Calanus pacificus*, *Metridia lucens* and *Pseudocalanus newmani* during a spring  
1038 bloom in Dabob Bay, a fjord in Washington USA. *J. Mar. Syst.* **15**, 503–509 (1998).
- 1039 30. Atkinson, A., Ward, P. & Murphy, E. J. Diel periodicity of Subantarctic copepods:  
1040 relationships between vertical migration, gut fullness and gut evacuation rate. *J.*  
1041 *Plankton Res.* **18**, 1387–1405 (1996).
- 1042 31. Visser, A. W., Grønning, J. & Jónasdóttir, S. H. *Calanus hyperboreus* and the lipid  
1043 pump. *Limnol. Oceanogr.* **62**, 1155–1165 (2017).
- 1044 32. Ohman, M. D. & Romagnan, J.-B. Nonlinear effects of body size and optical  
1045 attenuation on Diel Vertical Migration by zooplankton. *Limnol. Oceanogr.* **61**, 765–  
1046 770 (2016).

1047

1048

1049

1050

1051

1052

